ACS APPLIED MATERIALS & INTERFACES

www.acsami.org
Research Article

Targeted Ferroptosis-Immunotherapy Synergy: Enhanced Antiglioma Efficacy with Hybrid Nanovesicles Comprising NK Cell-Derived Exosomes and RSL3-Loaded Liposomes

Wenyan Hao, Nan Sun, Yueyue Fan, Mengyu Chen, Qianqian Liu, Meiyan Yang,* Yang Yang,* and Chunsheng Gao*

Cite This: ACS Appl. Mater. Interfaces 2024, 16, 28193−28208
Read Online

ABSTRACT: Ferroptosis therapy and immunotherapy have been widely used in cancer treatment. However, nonselective induction of ferroptosis in tumors is prone to immunosuppression, limiting the therapeutic effect of ferroptosis cancer treatment. To address this issue, this study reports a customized hybrid nanovesicle composed of NK cell-derived extracellular versicles and RSL3-loaded liposomes (hNRVs), aiming to establish a positive cycle between ferroptosis therapy and immunotherapy. Thanks to the enhanced permeability and retention effect and the tumor homing characteristics of NK exosomes, our data indicate that hNRVs can actively accumulate in tumors and enhance cellular uptake. FASL, IFN-γ, and RSL3 are released into the tumor microenvironment, where FASL derived from NK cells effectively lyses tumor cells. RSL3 downregulates the expression of GPX4 in the tumor, leading to the accumulation of LPO and ROS, and promotes ferroptosis in tumor cells. The accumulation of IFN-γ and TNF-α stimulates the maturation of dendritic cells and effectively induces the inactivation of GPX4, promoting lipid peroxidation, making them sensitive to ferroptosis and indirectly promoting the occurrence of ferroptosis. This study highlights the role of the customized hNRV platform in enhancing the effectiveness of synergistic treatment with selective delivery of ferroptosis inducers and immune activation against glioma without causing additional side effects on healthy organs.

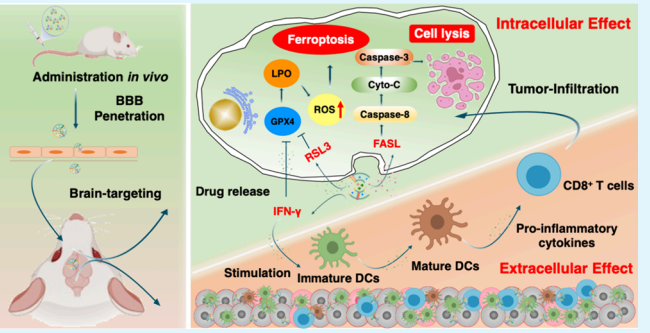

KEYWORDS: *natural killer cell, biomimetic hybrid nanovesicles, targeted delivery, enhanced ferroptosis therapy, immunotherapy*

1. INTRODUCTION

Glioma, the most aggressive form of brain tumor, is renowned for its high mortality rate, dismal prognosis, and recurrent nature.[1−3] Current therapeutic approaches are primarily limited to surgical resection followed by radiotherapy (RT) and adjuvant chemotherapy.[4] However, the blood−brain barrier (BBB) and blood−brain tumor barrier (BBTB) pose significant challenges in delivering chemotherapeutic agents to the central nervous system (CNS).[5−7] Additionally, prolonged chemotherapy usage often leads to drug resistance in glioma patients, thereby compromising therapeutic outcomes.[8,9] Ferroptosis therapy, a novel therapeutic approach, offers promising opportunities for cancer refractory to traditional treatments.[10,11] Ferroptosis is a complex and highly regulated process involving the dysregulation of iron homeostasis, glutathione (GSH) metabolism, and lipid peroxidation. Numerous studies have emphasized the crucial role of ferroptosis in various malignancies, including lung cancer, ovarian cancer, leukemia, and glioma.[12,13]

The intricate interplay between metabolic regulation and immune response governs the tumor microenvironment, often leading to metabolic disorders that either initiate or accelerate tumor growth.[14] Recent insights reveal a crosstalk between ferroptosis mechanisms in tumor cells and the immune system.[15,16] However, the nonspecific circulation of ferroptosis agents upon intravenous administration can lead to unintended cytotoxicity, affecting crucial immune cells like $CD8^+$ T cells, natural killer (NK) cells, and dendritic cells (DCs).[17,18] Additionally, the evasion of immune recognition by tumors due to a lack of activation factors hinders the specificity and clinical utility of these drugs. Therefore, there is an urgent need for innovative brain-targeted drug delivery systems that can efficiently traverse the blood−brain barrier (BBB) and blood−brain tumor barrier (BBTB) to deliver ferroptosis agents safely and effectively to tumor cells. This would enhance the

Received: March 20, 2024
Revised: May 10, 2024
Accepted: May 14, 2024
Published: May 22, 2024

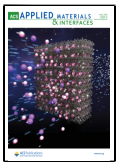

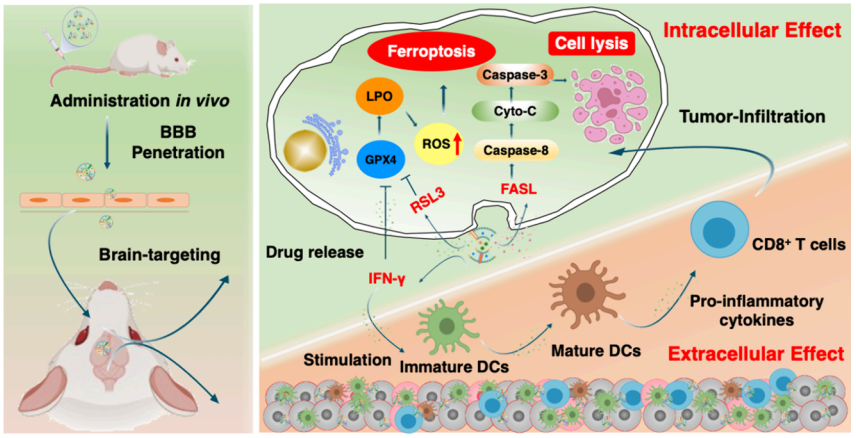

Figure 1. Schematic illustration of the action mechanism of hNRVs for synergistic ferroptosis-immunotherapy. After intravenous injection into glioma-bearing mice, hNRVs transmigrate to the brain across the BBB and BBTB and penetrate the infiltrating glioma cells. They actively accumulate in tumors, releasing immune activators and ferroptosis inducers, thereby exerting a synergetic ferroptosis-immunotherapy effect.

intracellular generation of reactive oxygen species (ROS) and lipid peroxidation (LPO) while simultaneously activating the immune response and remodeling the immunosuppressive tumor microenvironment (TME).[19,20]

Currently, ferroptosis is primarily achieved by inhibiting the cystine/glutamate antiporter system Xc^- and the GSH-GPX4 axis, resulting in the accumulation of lipid reactive oxygen species and subsequent cell death.[21,22] This process involves iron and lipid metabolism. Cystine plays a key role in GSH synthesis, reducing the level of lipid peroxide accumulation in cell membranes through GPX4 activity regulation. GSH deficiency can also deactivate GPX4, triggering ferroptosis.[22,23] Therefore, modulating iron metabolism and enhancing GPX4 expression via GSH concentration inhibition can accelerate tumor ferroptosis. RSL3, a GPX4 inhibitor, is commonly used to induce ferroptosis, but its clinical translation is limited due to poor water solubility, instability *in vivo*, and nonspecific distribution.[24] Efficiently delivering RSL3 to the tumor site is a crucial challenge. Liposomes, approved by the FDA for marketing,[17] are established drug carriers with excellent drug loading capacity. Encapsulating insoluble drugs in liposomes enhances drug stability and reduces toxicity. However, liposomes face challenges in circulation time and targeted delivery efficiency, similar to other nanomedicines.[20,25] Off-target toxicity is a common issue with traditional targeted modification strategies for liposomes.[26] Hence, there is an urgent need to develop a safe and effective liposome delivery system.

In recent years, strategies leveraging the body's pathophysiological mechanisms for targeted drug delivery have attracted researchers' attention. NK cells, innate lymphoid cells crucial in cancer immune response,[27] mediate cytotoxic effects via Fas death receptors and ligands like FASL, inducing caspase-dependent apoptosis. Additionally, NK cells secrete IFN-γ and TNF-α, triggering perforin release, suppressing tumor cell growth.[28] Beyond cytotoxic functions, NK cells recruit dendritic cells to solid tumors, enhancing $CD8^+$ T cell responses.[29−31] IFN-γ, in particular, can deactivate GPX4, enhancing lipid peroxidation in tumor cells, sensitizing them to ferroptosis.[32] Delivering cytokines such as FASL, IFN-γ, and TNF-α to lesions can eliminate $CD8^+$ T cell-evasive cancer cells and sensitize tumor cells to ferroptosis. This dual T cell and NK cell attack deepens immunotherapy's impact. However, traditional cell therapies struggle to treat solid tumors due to limited immune cell tumor penetration. NK cell-derived extracellular vesicles (NK-EVs), with nanoscale dimensions and superior tissue permeability, can cross the BBB for targeted brain tissue delivery. Yet, challenges like low EV extraction efficiency and uncontrollable drug loading hinder EVs' drug delivery applications.[33,34] Facing these challenges, hybrid nanovesicles have garnered significant attention in recent scientific advancements. Liposomes, spherical vesicles composed of phospholipid molecules, share a composition similar to EVs. Based on similarity-miscibility theory, this similarity suggests feasibility for membrane fusion between liposomes and NK-EVs. The integration of NK-EVs with liposomes offers a "1 + 1 > 2" synergistic effect.[35,36] This not only compensates for the limited drug loading capacity and uncontrollable drug loading process of exosomes but also endows the hybrid liposomes with the active targeting function of EVs, enabling BBB and BBTB traversal. Subsequently, drug release occurs, enhancing nanoparticle penetration into tumor tissues and minimizing cytotoxic effects and hypersensitivity reactions associated with liposomes.

Herein, we developed hybrid nanovesicles (hNRVs), a novel formulation combining RSL3-loaded liposomes with NK-EVs, designed to synergistically trigger ferroptosis and immunotherapy. As Figure 1 illustrates, these biomimetic nanovesicles possess a stable and uniform structure, exhibiting a high drug loading capacity and inheriting the biological attributes of NK-EVs. *In vivo* and *in vitro* studies confirm their ability to migrate effectively to tumor tissues, displaying remarkable therapeutic synergism. Leveraging the EPR effect and tumor homing properties of NK exosomes, hNRVs accumulate actively in tumors, enhancing cellular uptake. Upon entering the tumor microenvironment, they release FASL, IFN-γ, and RSL3. FASL lyses tumor cells, while RSL3, as a GPX4 inhibitor, triggers ferroptosis by disrupting redox homeostasis. IFN-γ and TNF-α further activate dendritic cells and sensitize tumor cells to ferroptosis. Additionally, necrosis- and ferroptosis-induced DAMPs activate $CD8^+$ T cells, augmenting immunotherapy. In summary, hNRVs facilitate targeted delivery of GPX4 inhibitors and immune activators, promoting synergistic immunotherapy and ferroptosis in tumors. This is the first design that utilizes NK cell-derived extracellular vesicles for synergistic ferroptosis and immunotherapy in tumor treatment,

https://doi.org/10.1021/acsami.4c04604
ACS Appl. Mater. Interfaces 2024, 16, 28193−28208

providing new insights for the clinical treatment and scientific research of NK cells in solid tumors.

2. MATERIALS AND METHODS

2.1. Materials. RSL3 was supplied by Shanghai Aladdin Biochemical Technology Co., Ltd. DCFH-DA and BODIPY C11-581/591 were supplied by Absin Bioscience, Inc. (Shanghai, China). The anti-CD86-FITC, anti-CD80-PE, anti-NKG2C, anti-CD4-FITC, anti-CD8-PE, and anti-ALIX antibodies and other antibodies used for flow cytometry assays were obtained from Abcam (Cambridge, UK). GPX4, GSH, TNF-α, IL-6, and IFN-γ ELISA kits were obtained from Absin Bioscience, Inc. (Shanghai, China). All other chemicals were sourced from Sigma-Aldrich. Unless otherwise stated, all chemicals were of reagent grade.

2.2. Cells and Experimental Animals. C6 glioma cells, RAW264.7 cells, bEnd.3 cells (mouse brain microvascular endothelial cells), and RBMVECs (rat brain microvascular endothelial cells) were supplied by the Cell Resource Center of IBMS (Beijing, China) and cultured in Dulbecco's modified Eagle's medium (DMEM) containing 10% fetal bovine serum (FBS; Gibco) and 100 IU of penicillin. Luciferase-tagged C6 glioma cells were purchased from the Cell Bank of the Chinese Academy of Sciences (Shanghai, China) and cultured in DMEM supplemented with 10% FBS at 37 °C in a humidified 5% CO_2 atmosphere.

Both male and female ICR mice (initially weighing 18−22 g) were provided by SPF Biotechnology Co., Ltd. All procedures involving the care and handling of animals were conducted with the approval of the Animal Care and Use Ethics Committee of the Beijing Institute of Pharmacology and Toxicology (Beijing, China). This committee also approved all animal-related experiments in the current study (No. IACUC-DWZX-2020-646).

2.3. The Extraction and Characterization of Activated NK Cells. Mouse NK cells were stimulated with TKD and IL-2 *in vitro*.[37] Briefly, peripheral blood lymphocytes of ICR mice were isolated by Ficoll-Paque gradient centrifugation and resuspended in an RPMI 1640 medium containing 2 mM glutamine and 10% FCS. Then, the peripheral blood lymphocytes were stimulated with TKD (20-mer) peptides and IL-2 (200 IU/mL) for 6 days at a cell density of 5×10^8/mL to obtain activated mouse NK cells (aNKs). Flow cytometry was performed on day 5 after TKD and IL-2 stimulation using a FITC-conjugated mouse CD16 antibody and a PE-conjugated monoclonal antibody against the NK cell activating receptor (NKG2C). The percentage of positive cells was determined after subtraction of cells stained with an isotype-matched negative control antibody. Only PI-negative live cells were gated and analyzed.

2.4. Preparation of NEVs, RLPs, and hNRVs. NK cell-derived extracellular vesicles (NK-EVs) were purified by differential centrifugation.[38] Briefly, the cell-conditioned medium was centrifuged for 15 min at 2500*g* to eliminate the residual cells and debris. The pellet was discarded, and the supernatant was first centrifuged for 20 min at 20,000*g*, recollected, and ultracentrifuged at 150,000*g* for 100 min. Supernatants were then discarded, and the exosome fraction was resuspended in PBS, frozen in liquid nitrogen, stored at −80 °C, and used within 1 week.

Liposomes were prepared by thin-film hydration.[39] Typically, RSL3, cholesterol, DSPE-mPEG 2000, and soy lecithin (molar ratio of 2:5:1:10) were added to 3 mL of dichloromethane, completely dissolved, and placed in a round-bottom flask, and the mixture was evaporated using a rotary evaporator under reduced pressure until a homogeneous lipid film was formed (37 °C, 100 rpm, 30 min). The obtained phospholipid film was then hydrated with 10 mL of ultrapure water for 30 min followed by sonication of the mixture with 50 W at 4 °C for 2 min. Homogeneous RLPs were obtained by centrifugation at 3000 rpm for 10 min and filtration through a 0.22 μm filter. The previously prepared RLPs, NK-EVs, and 60% (w/v) PEG8000 in phosphate-buffered saline (PBS) were thoroughly mixed at a volume ratio of 1:1:2 and incubated at 40 °C for 2 h to synthesize hNRVs. PEG8000 causes aggregation and adhesion of NK-EVs with RLPs.

2.5. Characterization of NK-EVs, RLPs, and hNRVs. The morphologies of NK-EVs, RLPs, and hNRVs were observed through transmission electron microscopy (TEM). First, NK-EVs, RLPs, and hNRVs were diluted in PBS. Each sample (10 μL) was then deposited onto an EM grid and observed under a TEM instrument at 100 kV. Dynamic light scattering (Litesizer 500, Anton Paar, Austria) was used to evaluate the size distribution and zeta potential. The hNRVs were stored in 1× PBS or PBS with 10% FBS at 37 °C. Stability analysis was performed by measuring the particle size and zeta potential over 7 days. The drug loading efficiency (LE) and encapsulation efficiency (EE) of hNRVs were determined by HPLC (Agilent 1200, USA).

2.6. Protein Analysis of NK-EVs and hNRVs. The expression of FASL and CD63 was examined through Western blot analysis. Notably, CD63 serves as a characteristic marker for extracellular vesicles derived from NK cells, while FASL represents a functional protein intimately linked to NK cells, as referenced in previous studies.[27,40,41] Initially, the NK-EVs, RLPs, and hNRVs were lysed using RIPA lysis buffer to extract proteins, which were then denatured at 95 °C for 5 min. Subsequently, the total protein concentration was determined using a BCA protein assay kit. The extracted proteins were blocked with Tris-buffered saline Tween buffer (TBST) containing nonfat dry milk for 1 h at 37 °C. Following this, they were incubated overnight at 4 °C with primary antibodies and then with peroxidase-conjugated secondary antibodies for 1 h at 37 °C. Finally, immunoreactive proteins were visualized using a gel imaging system.

2.7. Verification of hNRV Fusion. To determine whether RLPs were incorporated into NK-EVs, fluorescence resonance energy transfer (FRET) was first employed to verify membrane fusion. Briefly, two lipophilic dyes, namely, DiD (excitation/emission = 644/663 nm) and DiI (excitation/emission = 549/565 nm), were employed. The extrusion fusion method was utilized for fusion of the NK-EVs and RLPs. NK-EVs were stained with DiD and DiI, and with respect to NK-EV protein, the final ratios were 0.5 and 1.82 wt % for DiI and DiD, respectively. A solution containing the NK-EVs was then placed in the vial and stirred at 37 °C for 1 h. Afterward, a free dye was washed away by centrifuging the membrane at 10,000*g* for 15 min, three times. RLPs were added to the DiI/DiD-doped NK-EVs at RLP to NK-EV protein weight ratios of 4:1, 2:1, 1:1, and 0:1 followed by extrusion to complete membrane fusion. The fluorescence spectrum of each sample was read using a plate reader (Tecan Spark, Austria) with an excitation wavelength of 500−650 nm under different mixing ratios (RLPs/NK-EVs). The fluorescence recovery of the donor (NK-EVs) at a low emission peak (nm) was utilized to indicate the increased amount of fusion. In addition, to further validate the fusion of NK-EVs and RLPs, samples were imaged under a confocal laser scanning microscope (CLSM) (LSM 880, Zeiss, Germany).

2.8. RSL3 Loading and *In Vitro* Cumulative Release Study. RSL3 was loaded into RLPs or hNRVs through a remote loading method. Briefly, RLPs and hNRVs were prepared as described above. Then, different concentrations of RSL3 (100, 200, 400, 600, and 800 μg/mL) within 1 mL of PBS were added into RLPs and hNRVs and incubated for 30 min at 45 °C with constant stirring, while for hNRVs, drugs were loaded by 15 times repeated extrusion using a liposome extruder. The unencapsulated RSL3 was removed by a dialysis tube (MWCO, 3500 Da) in PBS. Then, the drug encapsulation efficiencies and loading capacities were determined by HPLC (Agilent 1200, USA).

The *in vitro* release of RSL3 was evaluated by the dialysis method. First, all RSL3-loaded samples were normalized to an RSL3 concentration of 100 μg/mL. Subsequently, 1 mL of nanoparticles was added to a dialysis tube (MWCO, 3500 Da) and immersed in 50 mL of PBS media (pH 6.8 or 7.4). Samples were shaken at a speed of 100 rpm at 37 °C on the shaker table. Release media (1 mL) were extracted at each predetermined time point and substituted with 1 mL of fresh media. The RSL3 concentration of the media was detected using HPLC (Agilent 1200, USA).

https://doi.org/10.1021/acsami.4c04604
ACS Appl. Mater. Interfaces 2024, 16, 28193−28208

2.9. *In Vitro* Cellular Uptake of hNRVs. Cells (bEnd.3, RBMVEC, and C6) were placed in 12-well plates (10^5 per well) and placed in a cell culture incubator overnight. DiI-labeled hNRVs in fresh DMEM were incubated with cells for 3 h. Then, cells were fixed with 4% paraformaldehyde for 15 min and rinsed with cold PBS 3 times. After the nucleus was stained by DAPI, cells were harvested and then resuspended in 300 μL of prechilled PBS followed by flow cytometer detection.

2.10. Absorption Inhibition Assay. Cells (bEnd.3 and C6) were seeded in 12-well plates (10^5 cells/well) and placed in a cell culture incubator overnight. The cells were then preincubated with inhibitors for 30 min followed by the addition of hNRVs for another 3 h. The inhibitors were dissolved completely in a phenol red-free medium. The inhibitors included 5 μM chlorpromazine, 50 μM dynasore hydrate, 10 μM cytochalasin D, 1 μM filipin, and 100 μg/mL amiloride hydrochloride.

2.11. *In Vitro* BBB and BBTB Model. bEnd.3 cells were cultured in the upper chamber of Transwell inserts, while C6 cells were cultured in the lower chamber for 7 days in DMEM supplemented with 10% FBS. Transendothelial cell resistance (TEER) values were measured to ensure the integrity of the cultured monolayer model,[42] thus creating a membrane that functions as the BBB. This created a membrane that acts as a BBB. Similarly, RBMVECs and C6 cells were employed to establish a BBTB model to investigate the penetration capacity of the preparations.

2.12. *In Vitro* Cytotoxicity and Apoptosis Analysis. The cytotoxicity of biomimetic hybrid nanovesicles was analyzed by using the standard Cell Counting Kit-8 (CCK-8) assay. In detail, C6 cells were seeded in a 96-well plate at a density of 5×10^5 cells/well. After being incubated for 24 h, the cells were treated with four formulations, namely, NK-EVs, RLPs, free RSL3, and hNRVs. The dose of RSL3 ranged from 0 to 15 μM, and the plates were incubated at 37 °C in a 5% CO_2 atmosphere for 48 h. After incubation for 48 h, 20 μL of a CCK-8 solution was added to each well, and the cells were cultured for 2 h. The absorbance of each well was measured at 450 nm using a microplate reader (Tecan Spark, Austria), and the IC_{50} of each formulation was calculated accordingly.

Annexin V-FITC/PI dual staining was used for analyzing apoptosis. C6 glioma cells were seeded in a six-well plate at 5×10^5 cells/well and cultured for 12 h. The cells were then treated with free NK-EVs, RLPs, free RSL3, and hNRVs (RSL3 dose at 5.3 μM). Following 48 h of incubation, the cells were collected, washed three times with cold PBS, suspended in 500 μL of a binding buffer, and stained with annexin V-FITC/PI. Finally, the cells were analyzed using flow cytometry (FACS Aria III, BD, USA). Nontreated cells were used as negative controls, and the experiment was repeated three times.

2.13. ROS and Lipid Peroxidation Assay. Cells were seeded in 6-well plates with a glass bottom and subjected to different treatments. The C11 BODIPY 581/591 assay kit and DCFH-DA assay kit were used following the manufacturer's manual. Results were analyzed by CLSM.

2.14. GPX4 Analysis *In Vitro*. C6 cells (5×10^5) were seeded in six-well plates cultured at 37 °C for 24 h. After 12 h, the cells were treated with four formulations, namely, NK-EVs, RLPs, free RSL3, and hNRVs, for 5 h. Afterward, the cells were washed with PBS three times followed by the addition of a fresh medium and cultured under hypoxia for another 12 h. The cells were then collected, and the GPX4 activity was analyzed using the commercial glutathione peroxidase assay kit (Beyotime Biotechnology, China). All procedures followed the product protocol ($n = 3$).

2.15. GSH Quantification. The *in vitro* GSH levels in C6 cells post formulation treatment were detected by a GSH assay kit under the manufacturer's protocol. C6 cells were seeded in six-well plates at 4×10^5 cells per well. After the cells reached 70−80% confluency, hNRVs were added to the culture medium, and the cells were collected after 12 h of incubation. The harvested cells were homogenized in a homogenizer on ice to obtain the disrupted cell dispersion. RLPs and NK-EVs were used as controls. The intracellular GSH content in untreated C6 cells was defined as 100%.

2.16. DC Maturation *In Vitro*. The effect of hNRVs on DC maturation was evaluated in Transwell systems. In brief, C6 cells at a density of 5×10^4 cells per well were seeded in the upper compartment, and DCs isolated from mice were seeded in the lower well at a density of 5×10^4 cells per well. After cell attachment, NK-EVs, RLPs, and hNRVs were added to the culture medium. After coincubation for 24 h, the DCs in the lower compartment were harvested by centrifugation and stained with anti-CD86-FITC and anti-CD80-PE for 30 min at 4 °C in the dark. After being washed with PBS three times, DCs were resuspended in PBS and analyzed by flow cytometry. At the same time, the culture medium in the supernatant after centrifugation was collected to measure the secretion of TNF-α and IL-6 by mature DCs. The levels of TNF-α and IL-6 were quantified by ELISA kits (Invitrogen) following the manufacturer's instructions.

2.17. Immune Escape Study. RAW264.7 cells were placed in 12-well plates (10^5 cells/well) and cultured for 12 h at 37 °C. DiI-labeled hNRVs in fresh DMEM were incubated with cells for 3 h. Afterward, cells were harvested and then resuspended in 300 μL of prechilled PBS followed by flow cytometry (Aria III, BD, USA).

2.18. Hemocompatibility Analysis. The hemocompatibility of the biomimetic hybrid nanovesicles was assessed based on a previously published protocol. Blood was collected from the eyes of healthy ICR mice and was collected in tubes containing heparin. After being centrifuged at 3000 rpm for 15 min, erythrocytes were obtained and washed three times with PBS. Then, pure erythrocytes at a ratio of 1:20 were diluted with PBS to prepare the 2% erythrocyte solution. Two hundred μL of hNRVs solution was added to the 2% erythrocyte suspension and incubated at 37 °C for 60 min, the mixed solution was centrifuged at 2000 r/min for 10 min at 4 °C to observe the color of the supernatant, erythrocyte lysis resulted in the release of hemoglobin, and the supernatant was collected and assayed at 540 nm to determine its absorbance. Two hundred μL of PBS (pH 7.4) and 200 μL of Triton X-100 solution were used as the negative control and positive control, respectively.

2.19. *In Vivo* Glioma Biodistribution. To investigate whether hNRVs could target glioma cells, intracranial glioma mouse models were established according to previously described procedures.[43,44] The glioma mouse model was established by following the procedure described previously. Briefly, after anesthetizing mice with chloral hydrate (4%, w/v), 2 μL of C6 cells at a density of 2×10^6 cells/mL was injected into the right striatum (1.8 mm lateral, 1 mm longitudinal, and 4 mm depth) of ICR mice. After 2 weeks, the mice were divided randomly into 4 groups and then intravenously injected with free DiR, RLPs, NK-EVs, and hNRVs at an RSL3 concentration of 2 mg/kg. Subsequently, DiR (1 mg/kg), serving as a fluorescent probe, was employed to label the diverse nanovesicles, which were subsequently intravenously administered into glioma-bearing mice. The biodistribution was monitored by fluorescence in each group using an *in vivo* spectrum imaging system (IVIS Spectrum, PerkinElmer, USA) with excitation and emission wavelengths of 748 and 780 nm. In addition, to further verify the tumor targeting ability of hNRVs to the tumor site, the glioma-bearing model mice were sacrificed at 12 h, and different organs, including the brain, heart, liver, spleen, lung, and kidney, were harvested. The region of interest (ROI) was circled around the tissues, and the fluorescence intensity was determined by using Living Image software.

For tumor distribution analysis, DiI (0.5 mg/kg) was used as the fluorescent probe. Glioma-bearing mice were intravenously injected with free DiI-labeled hNRVs. After treatment for 4 h, brain tissues were removed and fixed with 4% paraformaldehyde in the dark for 24 h. DAPI, which was observed at an excitation wavelength of 358 nm and an emission wavelength of 461 nm, was used to stain the nuclei. Finally, the distribution of hNRVs in each brain tissue section was observed by using an inverted fluorescence microscope.

2.20. *In Vivo* Pharmacokinetics Study. To evaluate the circulating half-lives of RLPs and hNRVs, DiI-labeled nanoparticles were injected into ICR mice via the tail vein. Blood samples of 30 μL were collected at 0, 5, 15, and 30 min and 1, 2, 4, 8, 24, and 48 h postinjection. Six mice were included in each group. The collected

https://doi.org/10.1021/acsami.4c04604
ACS Appl. Mater. Interfaces 2024, 16, 28193−28208

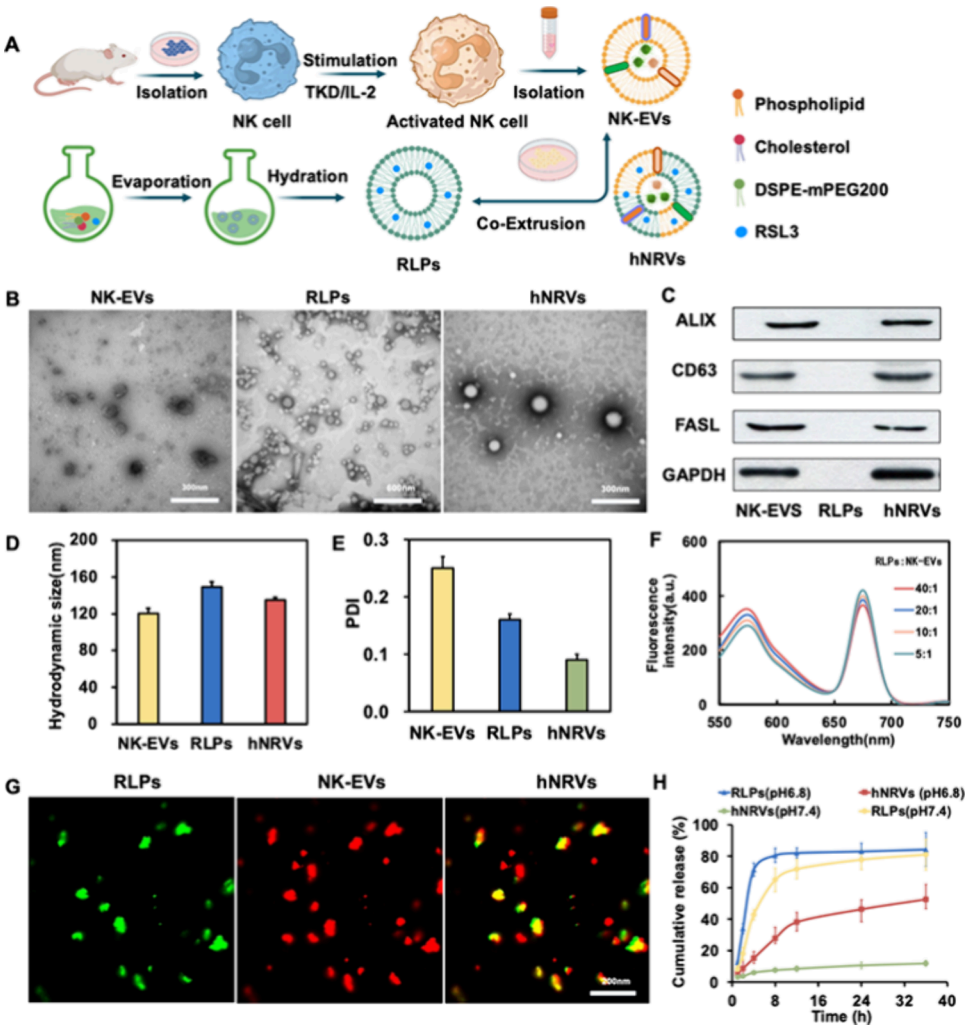

Figure 2. Characterization of hNRVs. (A) Fabrication of hNRVs. (B) Representative TEM images of NK-EVs, RLPs, and hNRVs. (C) Western blotting of NK extracellular vesicle-specific protein on NK-EVs, RLPs, and hNRVs. (D) Hydrodynamic size distribution and PDI (E) of different formulations. (F) Validation of hybridization via FRET analysis and CLSM images (G). (H) Cumulative release of RLPs and hNRVs in different release media (n = 3). Data were presented as means ± SD; *p < 0.05, **p < 0.01, and ***p < 0.001; ns, not significant.

blood samples were diluted in a 96-well plate with 70 μL of PBS, and then, fluorescence measurements were taken using a microplate reader (Tecan Spark, Austria). A standard curve was generated by mixing DiI with hNRV solution, diluting the mixture to concentrations of 2, 4, 10, 20, and 50 μg/mL, and subsequently measuring the correlation between fluorescence intensity and DiI concentration.

2.21. Antitumor Experiments *In Vivo*. To monitor tumor growth intuitively, the mice were intracranially implanted with Luc-C6 cells (1×10^5cells/mouse), and models of intracranial glioma mice were established according to a previous procedure. The mice were randomly divided into five groups (n = 4): NK-EVs, RLPs, free RSL3, hNRVs, and the control group treated with PBS.

All preparations were intravenously injected into the mice every 3 days for a total of five administrations, with an RSL3 dose of 2 mg/kg. On days 0, 7, 14, and 21 after administration, bioluminescence imaging of the tumor was conducted 10 min following an intraperitoneal injection of D-luciferin at a dose of 150 mg/kg. The body weight of the mice was measured every 2 days after treatment. The survival period of the mice was recorded throughout the experiment, with any deaths or pathologic events being promptly noted. After 20 days of administration, three mice from each group were randomly selected and sacrificed, and their brains were collected and fixed in 4% paraformaldehyde for 48 h for subsequent H&E and TUNEL staining to assess the degree of tumor cell apoptosis.

2.22. *In Vivo* Synergistic Mechanism Evaluation of Ferroptosis-Immunotherapy. To evaluate the synergistic ferroptosis-immunotherapy mechanism *in vivo*, the glioma-bearing ICR mice were divided into five experimental groups and treated three times at intervals of 1 week by intravenous injection with PBS (control), RSL3, RLPs, NK-EVs, and hNRVs at an equal amount of RSL3 (2 mg/kg). After 14 days, tumor tissues and lymph nodes were collected. Tumor cells were stained by BODIPY C11-581/591 and DCFH-DA to determine the level of intratumoral LPO and ROS accumulation. In addition, the tumor tissues were homogenized for obtaining the supernatant. The expression of TNF-α, IFN-γ, GPX4, and GSH in tumors was detected using an enzyme-linked immunosorbent assay (ELISA). In addition, immunohistochemical (IHC) staining was conducted on brain tissues to determine the expression of caspase-3 and cytochrome-C protein. The infiltration of $CD8^+$ and $CD4^+$T lymphocytes in tumor tissues was analyzed via immunofluorescence staining. Dendritic cells (DCs) in the lymph nodes were stained with APC anti-CD80 and PE anti-CD86 antibodies to determine the ratio of matured DCs.

2.23. Histology and Immunohistochemistry. The collected mouse tissues were fixed in 4% paraformaldehyde in a PBS buffer overnight. They were then gradually dehydrated in ethanol, transferred to xylene, and embedded in paraffin. The paraffin-embedded tissues were cut into 4 μm-thick sections and histologically examined by H&E staining and immunohistochemistry (IHC).

https://doi.org/10.1021/acsami.4c04604
ACS Appl. Mater. Interfaces 2024, 16, 28193−28208

2.24. Immunofluorescence Staining. The samples with various treatments were gently washed three times with PBS, fixed with 4% paraformaldehyde for 15 min, and rinsed with PBS 3 times for 3 min each. Cells were then permeabilized using 0.3% Triton X-100 for 15 min and washed with PBS 3 times for 3 min each. An animal nonimmune serum was added dropwise to the cells or tissues for blocking. Then, the samples were incubated at room temperature for 1 h. The primary antibody at the optimal working concentration was added dropwise to the tissue or cell, incubated at 37 °C for 1 h, and rinsed with PBS 3 times for 5 min each. Fluorescent secondary antibodies were then added for incubation at room temperature for 1 h in the dark and rinsed with PBS 3 times. Then, the nucleus was stained with DAPI for 10 min. Finally, the samples were washed with PBS and observed by CLSM (LSM 880, Zeiss, Germany).

2.25. Biosafety Evaluation. For biocompatibility and biosafety *in vivo* analysis, normal male mice were randomly divided into four groups and intravenously injected with 200 μL of saline (control), RLPs, NK-EVs, and hNRVs. Sixteen days later, all mice were euthanized, and serum samples from the mice were collected to detect alanine transaminase (ALT), aspartate transaminase (AST), and creatinine (CREA). Further, the heart, liver, spleen, lung, kidney, and brain were removed for histology via H&E staining. The body weights of mice during treatments were measured every 2 days.

2.26. Statistical Analysis. All experiments were conducted in triplicate and expressed as the mean ± the standard deviation. Statistical significance was analyzed using SPSS 19.0 (IBM Corp., Armonk, NY, USA). One-way analysis of variance with *post hoc* Tukey's test was used to determine significant differences between data sets.

3. RESULTS AND DISCUSSION

3.1. Preparation and Characterization of hNRVs. First, we isolated and prepared activated NK cells from peripheral blood lymphocytes as previously described[38] (Figure 2A). NKG2C and CD16 have been reported to be expressed in activated NK cells.[45−47] The aNKs that we prepared were positive for NKG2C and CD16 (Figure S1A,B), indicating the potential of expressing lytic granules such as FASL and perforins. Next, NK-EVs were prepared isolated via a differential centrifugation method. The purity of NK-EVs was examined by TEM, revealing that NK-EVs were spherical particles of 120 ± 5.5 nm with an intact membrane structure, consistent with the well-established characteristics of EVs (Figure 2B). Further characterization of NK-EVs by Western blot analysis confirmed the presence of two typical exosome proteins, namely, CD63 and ALIX.[45−47] NK cells are known to exert their cytotoxic activity through the release of cytotoxic cytokines contained in lytic granules. At the same time, several transmembrane proteins, such as FASL, are exposed on the cell surface and dictate the fates of effector and target cells. Thus, we confirmed the presence of FASL in NK-EVs through Western blot analysis (Figure 2C). The average protein concentration of NK-EVs was 68.3 μg/mL detected by a BCA kit following the manufacturer's procedure. In addition, we found less protein loss caused by extrusion and sonication during preparation (Figure S1C). Next, RLPs were prepared by using a film dispersion method. The prepared RLPs were 149 ± 6.0 nm in diameter. Finally, hNRVs were successfully prepared by using the extrusion method. DLS measurements showed that the particle size of hNRVs was 135 ± 2.7 nm (Figure 2D). The nanoscale size can benefit the substantial accumulation of hNRVs in the tumor via the enhanced permeability and retention (EPR) effect. In addition, the decreased polydispersity index (PDI) indicated that hNRVs possessed a better size homogeneity than NK-EVs (Figure 2E). A possible explanation is that the insertion of a lipid membrane led to the dilution of the hNRV surface protein corona and reduction of protein−protein interaction-induced aggregation. There was a decreased zeta potential of hNRVs (−29.6 ± 3.5 mV) compared with PLPs (−26 ± 2.2 mV), probably due to the insertion of NK-EV membrane lipids (−30.3 ± 3.1 mV) (Figure S1D).

Stability is a prerequisite for the further application of hNRVs *in vivo*. The stability of the biomimetic hybrid nanovesicles was evaluated in both PBS and PBS containing 10% FBS over a period of 7 days at 37 °C to mimic the *in vivo* conditions. As shown in Figure S1E,F, hNRVs showed little protein adsorption and negligible changes in particle size after incubation with 10% FBS, indicating that hNRVs could exhibit effective immune evasion *in vivo*. These results confirmed that the fusion of NK-EVs and RLPs effectively prevented the absorption of plasma proteins and enhanced the plasma stability of the nanoparticles. Superior plasma stability would enhance the nanoparticles' immune escape ability and maintain their stability in blood circulation *in vivo*. These results further demonstrated the potential of hNRVs for drug delivery and multiple cytokine delivery.

3.2. Validation of Hybridization. The successful fusion of RLPs and NK-EVs is paramount to the effective delivery of drugs and cytokines via hNRVs. Therefore, the hybridization assay was initially conducted. To assess the fusion, NK-EVs were doped with two distinct dyes, forming a FRET pair. Our observations revealed that fluorescence resonance occurred at 578 nm. Notably, as the quantity of RLPs increased, a recovery of fluorescence was observed at an approximately 675 nm emission wavelength. This finding indicates the fusion of the two membrane materials, leading to the attenuation of FRET interactions within the original NK-EVs (Figure 2F). Subsequently, CLSM imaging was employed to further corroborate the fusion of various nanovesicles (Figure 2G). NK-EVs and RLPs were mixed in a protein weight ratio of 5:1. Specifically, the RLPs labeled with the red fluorescent dye (DiI) fused with NK-EVs were labeled with a green fluorescent dye (DiD). The merged fluorescence exhibited colocalization of RLPs-DiI and NK-EVs-DiD, unequivocally demonstrating the cofusion of the liposomal membrane and NK-EV membrane. Collectively, these results unequivocally confirm the successful formation of hNRVs.

3.3. Drug Loading and *In Vitro* Release Study. To achieve a high encapsulation efficiency of RSL3 in hNRVs, the remote loading method was employed here.[48] As a comparison, RLPs were also prepared accordingly. The results demonstrated that the high drug encapsulation efficiency (>95%) in hNRVs was obtained even at the initial feed concentration of RSL3 (800 μg/mL), and the loading efficiency gradually increased from 2.8 to 27.2% with the increased initial RSL3 feed (Figure S1G). The RLPs exhibited a drug loading profile comparable to that of hNRVs, suggesting that the integration of the NK-EV membrane did not significantly affect the drug loading efficiency (Figure S1H). During our study, through a rigorous process of formulation screening and process optimization, we achieved a drug loading capacity of 5.6% for RSL3 in the RLPs. Additionally, using ELISA kits, we measured the concentrations of FASL and IFN-γ in the extracted NK exosomes, which were found to be 47.44 and 26.03 pg/mL, respectively. Subsequently, we fused the RLPs with NK-EVs to obtain the hybrid nanovesicles (hNRVs). After fusion, the drug loading of RSL3 in hNRVs was detected to be 4.8 ± 1.64%. Correspondingly, the

https://doi.org/10.1021/acsami.4c04604
ACS Appl. Mater. Interfaces 2024, 16, 28193−28208

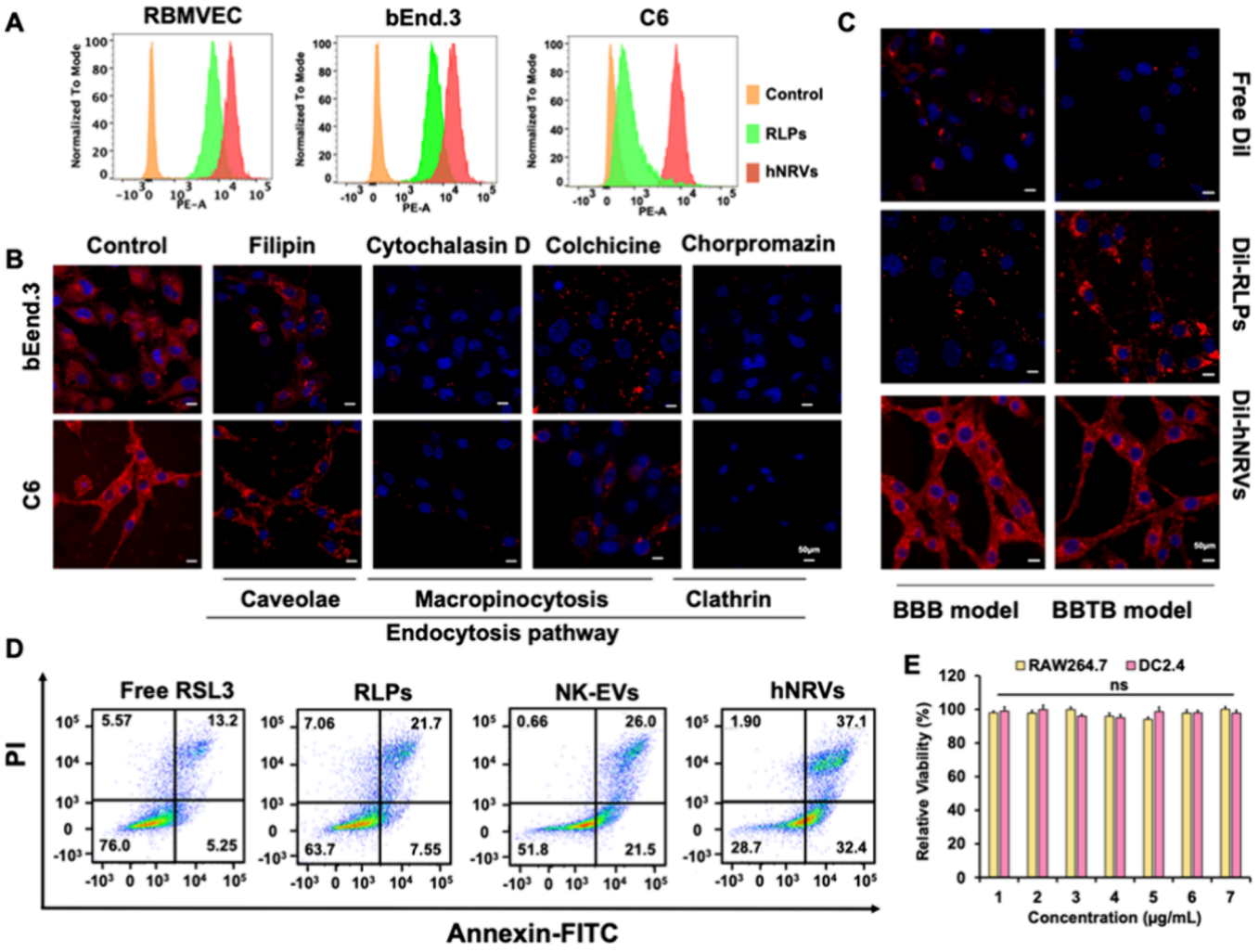

Figure 3. Assessment of cellular uptake behavior and cytotoxicity of hNRVs. (A) Flow cytometry of uptake efficiency of hNRVs by different cells. (B) Representative CLSM images and quantification of the cellular uptake of hNRVs in cells treated with PBS, filipin, cytochalasin D, colchicine, and chlorpromazine. DiI: red; DAPI: blue. (C) *In vitro* BBB and BBTB model penetration analysis. (D) Cell apoptosis induced by various treatments examined by flow cytometry. The cells were stained with annexin V-FITC and PI. (E) Viability of RAW264.7 and DC2.4 cells in response to different concentrations of hNRVs. Data were presented as means ± SD; $*p < 0.05$, $**p < 0.01$, and $***p < 0.001$; ns, not significant.

concentrations of FASL and IFN-γ were 43.01 and 23.76 pg/μg, respectively. These results indicate that there was a minimal loss of active ingredients during the fusion process, ensuring the efficiency of our drug delivery system.

To mimic the release profiles of RSL3 *in vivo*, the drug release kinetics of both hNRVs and RLPs were assessed at 37 °C for 36 h in media with pH 6.8 to mimic the acidic tumor environment and pH 7.4 to represent a normal physiological environment.[42,49] As exhibited in Figure 2H, RLPs demonstrated obvious burst release in different release media. The cumulative release of RSL3 from RLPs reached 43% within 4 h, with release amounts of 81% at pH 7.4 and 84% at pH 6.8 within 36 h. However, hNRVs exhibited only a 12% RSL3 release at pH 7.4 within 36 h, whereas at pH 6.8, up to 53% release occurred within 4 h. This indicated that hNRVs are more stable than RLPs under normal physiological conditions (pH 7.4) but are sensitive to the mildly acidic tumor microenvironment. The pH-triggered release characteristic was probably attributed to the destabilization of the lipid carrier and increased solubility of RSL3 under acidic conditions. The results further indicated that the fusion of NK-EVs with the RLP membrane significantly enhanced the drug loading stability.

3.4. Enhanced Internalization and Cytotoxicity of hNRVs *In Vitro*. Cellular uptake is a prerequisite for both drug and exosome delivery. RBMVECs, bEnd.3 cells, and C6 cells are key components of the BBB and BBTB. The cellular uptake behavior of different preparations in normal media was conducted. As shown in Figure 3A, the uptake efficiency of hNRVs by bEnd.3 cells was 3−4 times higher than that of RLPs, and the uptake efficiency in RBMVECs and C6 cells showed similar differences. To further confirm the internalization behavior of hNRVs, we individually treated cells with various endocytosis inhibitors including filipin, cytochalasin D, colchicine, and chlorpromazine. Filipin is a caveola-mediated endocytosis inhibitor. Cytochalasin D is a macropinocytosis inhibitor. Colchicine interferes with microtubule trafficking by binding to tubulin subunits and blocking macropinocytosis. Chlorpromazine blocks the clathrin endocytosis pathway.[50−52] As shown in Figure 3B and Figure S2A,B, the cellular uptake of hNRVs by C6 glioma cells and bEnd.3 cells was affected by most of the inhibitors and was significantly suppressed by cytochalasin D and chlorpromazine, indicating that hNRV

https://doi.org/10.1021/acsami.4c04604
ACS Appl. Mater. Interfaces 2024, 16, 28193−28208

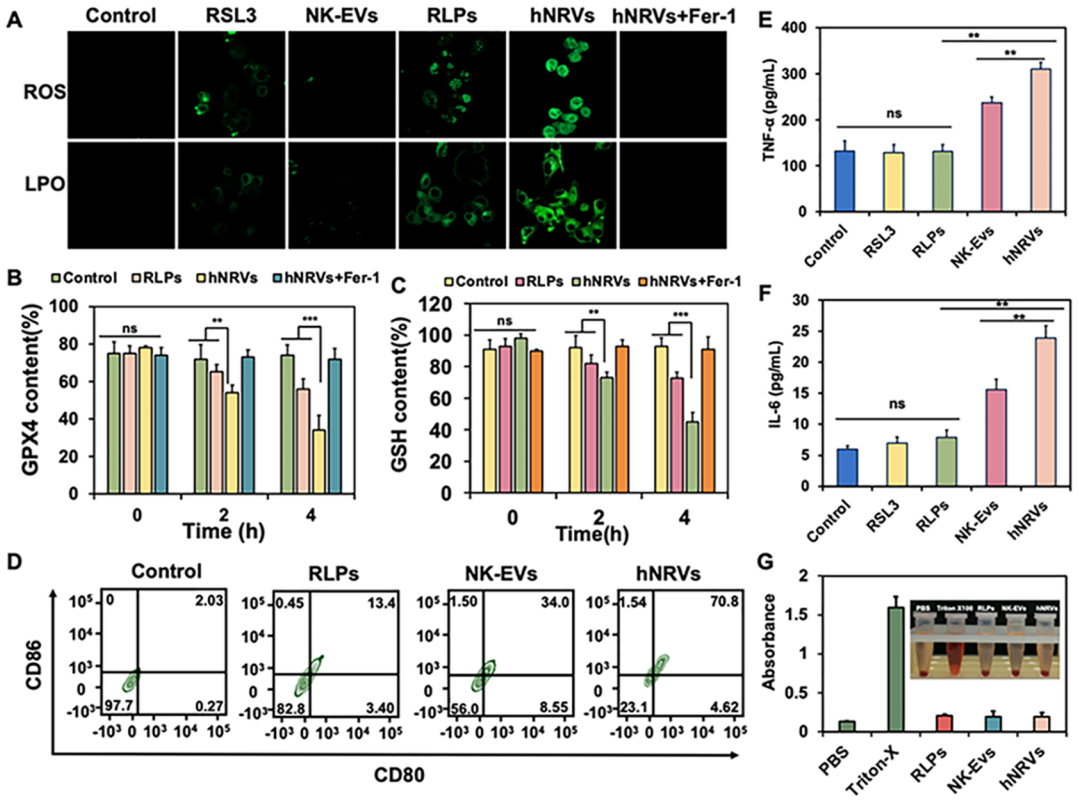

Figure 4. hNRV-induced ferroptosis and activation of BMDCs *in vitro*. (A) ROS and LPO imaging in C6 cells. (B) GPX4 level and GSH level (C) in C6 cells post hNRV incubation. (D) BMDC maturation as detected by FC with staining of anti-CD80 and anti-CD86. (E) TNF-α and IL-6 (F) levels in the supernatants of BMDCs with different treatments. (G) *In vitro* hemocompatibility of hNRVs. Data were presented as means ± SD; *p < 0.05, **p < 0.01, and ***p < 0.001; ns, not significant.

uptake by C6 cells and bEnd.3 cells was multifaceted and the endocytosis of hNRVs was internalized mainly by clathrin and micropinocytosis.

The ability of the drug to travel across the BBB is the key to treatment of brain diseases.[53,54] Transwell models were used to evaluate the ability of hNRVs to cross the BBB and BBTB *in vitro*. Monolayer culture in a Transwell with bEnd.3 cells or HUVECs in the upper chamber and C6 cells in the lower chamber is commonly used in *in vitro* models for brain delivery studies.[44,55] An *in vitro* BBB model with a barrier function was established using bEnd.3/C6 glioma cells. The TEER value is an important indicator for evaluating the integrity of the BBB model. In the experiments, the successful construction of the model was initially determined by a TEER value greater than 200 Ω·cm^2.[42] The selection of this threshold is based on literature reports and previous experience in our laboratory, which indicates that the BBB model has a good barrier function and can effectively simulate the permeability of the blood−brain barrier *in vivo*.[45] During the experimental process, although the initial TEER value of the constructed BBB model met the requirements, in order to ensure the integrity of the entire experimental process, we believe that it is very necessary to measure the TEER value again at critical stages of the experiment, including before and after drug treatment and detection. These detections all showed TEER values greater than 200, indicating that the BBB was intact.

CLSM results showed that the fluorescence intensity of the hNRV and NK-EV groups was stronger than that of the free DiI group, indicating that hNRVs preserved the specific BBB targeting ability from NK cells. The HUVEC/C6 cell coculture model was used as the BBTB, and the resistance value was 233.5 Ω·cm^2. Compared with other groups, hNRVs also showed the greatest tumor targeting ability, further indicating that the fusion of NK-EVs and RLPs could enhance the ability of hNRVs to penetrate the BBB and BBTB (Figure 3C and 2Figure S2C).

Afterward, the *in vitro* synergistic anticancer activity was determined using the CCK-8 assay (Figure S2D). All preparations (NK-EVs, RLPs, and hNRVs) exhibited prominent cytotoxicity with an IC_{50} of 5.1 μg/mL, which was much lower than that of RSL3 (36.7 μg/mL), confirming the excellent RLP- and NK-EV-induced antitumor performance. Free RSL3 exhibited faint suppression on the proliferation of glioma cells, which illustrates that interfering tumor ferroptosis metabolism alone hardly effectively caused a good antitumor effect. Compared with NK-EVs, hNRVs had greater inhibition on the proliferation of C6 cells. It manifested that the synergy of tumor ferroptosis metabolism regulation and immunotherapy by employing hNRVs had the most anticancer therapeutic effect. Similar results were also observed in the apoptosis flow cytometry assay. As shown in Figure 3D, the groups including free RSL3 and RLPs produced weak apoptosis. Compared to other groups, hNRVs exhibited the highest degree of apoptosis, with 66.3 ± 3.2% of the total apoptosis ratio. In contrast, the total apoptosis ratios in the groups (RSL3, RLPs, and NK-EVs) were 18.3 ± 1.1, 28.4 ± 2.3, and 47.2 ± 1.7%, respectively. The cytotoxicity of hNRVs was also evaluated on RAW264.7 and DC2.4 cells using the CCK-8 assay. In comparison with direct cytotoxicity on tumor cells, RLPs and hNRVs both produced slight cytotoxicity even at a high RSL3

https://doi.org/10.1021/acsami.4c04604
ACS Appl. Mater. Interfaces 2024, 16, 28193−28208

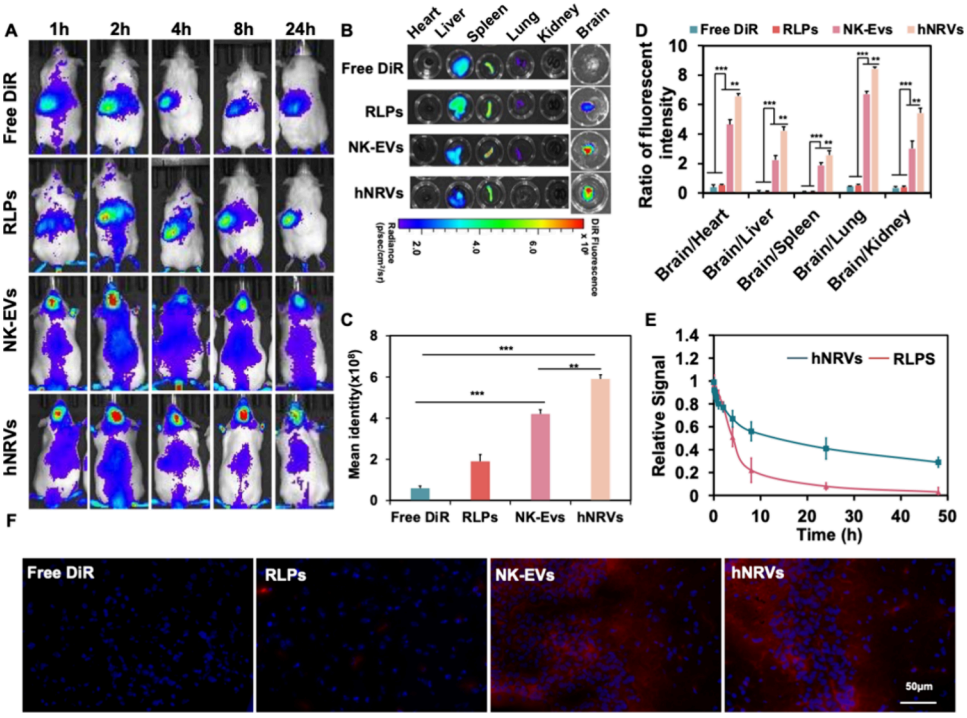

Figure 5. *In vivo* glioma targeting and biodistribution of hNRVs. (A) Living images of glioma-bearing mice with different treatments. (B) Fluorescence imaging in different organs and brain tissues (C). (D) Ratio of fluorescence intensity in brain tissues and different organs. (E) Pharmacokinetics behavior of RLPs and hNRVs in glioma-bearing mice. (F) Immunofluorescence staining of hNRVs in glioma-bearing brains at 12 h after administration. Data were presented as means ± SD; $*p < 0.05$, $**p < 0.01$, and $***p < 0.001$; ns, not significant.

concentration of 7 μg/mL in normal physiological conditions, indicating that RSL3-loaded nanovesicles showed a relatively safe profile on RAW264.7 cells and DC2.4 cells (Figure 3E). The enhanced cellular uptake and selective cell cytotoxicity of this hybrid nanovesicle may make it a promising delivery system for cancer nanomedicine.

3.5. hNRVs Induce Ferroptosis *In Vitro*. The DCFH-DA was utilized to stain the C6 cells to specifically identify the generation of intracellular ROS, which induces ferroptosis. Figure 4A shows the CLSM images of the C6 cells treated with the DMEM medium (control), RLPs, NK-EVs, and hNRVs and stained with DCFH-DA (green). Both RLP and hNRV groups present robust green dots, indicating the increase of the intracellular ROS level. Compared with the control group, the RLP and hNRV groups show much stronger green fluorescence ($p < 0.001$). The hNRV group was more potent than the RLP group in ROS production, primarily because of the enhanced cellular uptake. Importantly, the intracellular ROS levels recovered to the same level as the control group with addition of ferroptosis inhibitors. Next, the treated C6 cells were stained with BODIPY C11-581/591 to determine the intracellular LPO level by CLSM. From Figure 4A, it is found that the intracellular level of LPO in the C6 cells treated with hNRVs also significantly increases compared with the other groups. Similarly, the LPO level in the cells treated with hNRVs with addition of Fer-1 is comparable to that of the control group, which is in accordance with the above-mentioned ROS results. It is obvious that the hNRVs could accelerate the accumulation of LPO. These results reinforce the critical role of hNRVs in ferroptosis induced in glioma. Figure 4B shows GPX4 levels in the C6 cells measured by ELISA after various treatments. The C6 cells treated with hNRVs and RLPs exhibit an obvious decrease in the GPX4 level, compared with the control and NK-EV groups. However, the GPX4 level in the cells treated with hNRVs with addition of Fer-1 shows a significant recovery. From Figure 4C, we find that the intracellular level of GSH (an important substrate of GPX4) in the C6 cells treated with hNRVs also significantly decreases compared with the control and NK-EV groups. Similarly, the GSH level in the cells treated with hNRVs with addition of Fer-1 is comparable to that of the control group, which is in accordance with the above-mentioned GPX4 assay results. Therefore, it can be concluded that hNRVs can be used for ferroptosis therapy of tumors. Therefore, hNRVs are promising to be used for tumor ferroptosis therapy via lipid peroxidation and redox imbalance induced by the high level of intracellular RSL3 and cytokines.

3.6. hNRVs Induce Maturation of Dendritic Cells *In Vitro*. We employed a Transwell device to coculture C6 cells and immature dendritic cells (imDCs) in the upper and lower chambers to mimic the complex tumor microenvironment (Figure S2F). The mouse bone marrow dendritic cells (BMDCs) were employed. The subpopulation of $CD86^+$/$CD80^+$ cells was used as the marker of the maturation of DCs (Figure 4D). It is found that NK-EV- or hNRV-treated C6 cells can obviously promote BMDC maturation compared with the control. The former is due to the fact that hNRVs can aid in the internalization of NK-derived cytokines by DCs, thereby directly promoting BMDC maturation. The latter is due to immunogenic cell death (ICD) resulting from cancer cell fragments generated by ferroptosis and necrosis induced by hNRVs, which can also promote DC maturation.[48,56] In addition, it can be seen that BMDC maturation is much higher in the presence of hNRVs compared to the NK-EV group, displaying "1 + 1 > 2" of synergistic effects in BMDC

https://doi.org/10.1021/acsami.4c04604
ACS Appl. Mater. Interfaces 2024, 16, 28193−28208

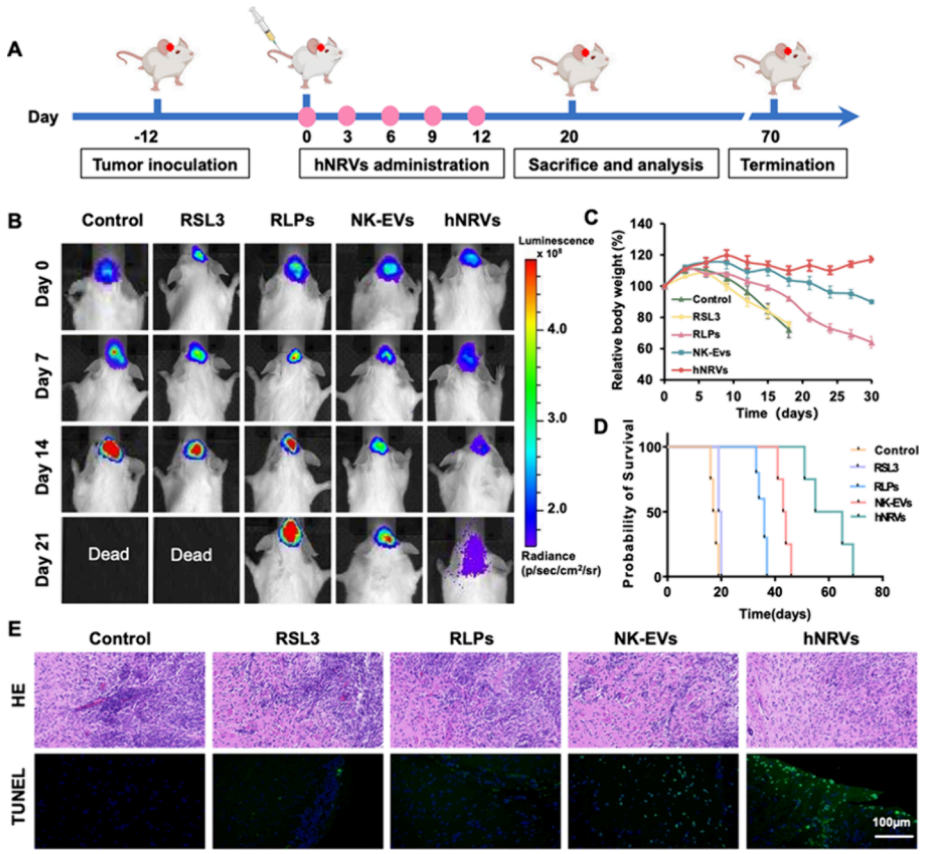

Figure 6. *In vivo* antiglioma efficacy of hNRVs. (A) Schematic illustration of the establishment of the orthotopic glioma-bearing mouse model and dose regimen. (B) Luciferase luminescence levels of mice following the indicated different treatments. (C) Body weight changes of mice in different treatment groups. (D) Survival rate of mice treated with different formulations. (E) H&E and TUNEL staining of tumor tissues after treatment with different formulations. Data were presented as means ± SD.

activation. Therefore, it can be concluded that hNRVs can be used for synergistic ferroptosis-immunotherapy of glioma.

The mature DCs (mDCs)would release proinflammatory cytokines, such as tumor necrosis factor-alpha (TNF-α) and interleukin-6 (IL-6).[56] Due to peroxidation and ferroptosis, the C6 cells undergoing ferroptosis would release immunostimulatory signals, triggering the maturation of imDCs (Figure S11, Supporting Information). There was a substantial release of TNF-α and IL-6 from BMDCs post hNRV treatment (Figure 4E,F), which corroborated the maturation of imDCs. Meanwhile, the targeted hNRVs were more potent than other groups in triggering cytokine release. The concentration of TNF-α was consistent with that of IL-6. Altogether, the targeted hNRVs could efficiently induce DC maturation in a Transwell coculture model.

3.7. Immune Escape and Hemocompatibility of hNRVs. We investigated the effect of hNRVs on the uptake by the reticuloendothelial system (RES). Comparing the uptake efficiency of RLPs and hNRVs by RAW264.7 cells, we found that the uptake efficiency of hNRVs was significantly reduced. After incubation with macrophages for 6 h, the number of internalized hNRVs was less than half that of RLPs (Figure S2E). NK-EVs have been reported to express CD47, a "don't eat me" signaling protein, indicating that the uptake of hNRVs by RES was reduced with CD47 blocking.[57] Next, a hemolytic assay was performed to evaluate the hemocompatibility of hNRVs. As shown in Figure 4G, hNRVs showed a negligible influence on erythrocytes and hardly produced a strong hemolytic effect, which reflects good biocompatibility.

3.8. *In Vivo* Brain Distribution and Pharmacokinetics. To examine the *in vivo* biodistribution of hNRVs, we employed a glioma-bearing mouse model. The DiR-labeled RLPs or hNRVs, at a DiR-equivalent dose of 2.5 mg/kg, were administered to track the biodistribution. At predetermined time intervals, the tumor and main organs were obtained and imaged under an *in vivo* imaging system (IVIS). Figure 5A shows that almost no free DiR and RLP fluorescence was detected at the brain tumor site, while other treatment groups showed different degrees of fluorescence signals. The accumulative fluorescence intensity in the tumor increased over time. Among these groups, the hNRVs showed much stronger fluorescence intensity than the NK-EV group after 4 h, showing that there were more hNRVs accumulated and retained in the tumor due to the specific targeting ability and EPR effect.[58] However, the lower brain accumulation observed for NK-EVs compared with hNRVs does not necessarily indicate a reduced targeting capacity. This observation can be explained by the differences in the physicochemical properties and stability of these two formulations. When NK-EVs are fused with RLPs to form hNRVs, the resulting system maintains the same amount of exosome protein as the standalone NK-EVs. This ensures that the targeting function of NK-EVs is not compromised by the fusion process. In fact, the fusion of NK-EVs with liposomes enhances the stability of the overall system. The addition of PEG to the liposomes

https://doi.org/10.1021/acsami.4c04604
ACS Appl. Mater. Interfaces 2024, 16, 28193−28208

confers long-circulating properties, which further enhances the EPR effect, allowing for improved accumulation in the tumor. Moreover, our stability studies and pharmacokinetic data support this hypothesis. These data demonstrate that the hNRV formulation is more stable than standalone NK-EVs, resulting in improved retention and distribution within the tumor. This stabilization effect, combined with the EPR enhancement, likely contributes to the observed higher accumulation of hNRVs in the brain compared to NK-EVs. We also collected the hearts, livers, spleens, lungs, kidneys, and brains of mice treated with different DiR-labeled formulations and investigated their distribution in each organ (Figure 5B). The strong DiR-NK-EV and DiR-hNRV fluorescence was observed in the brain and localized to brain tumor locations. Quantitative analysis of the brain tissue further confirmed the brain targeting effect of the hNRVs. Furthermore, we quantitatively analyzed the proportion of the hNRV content in the brain compared to other major organs to confirm the brain delivery characteristics of hNRVs (Figure 5C,D). The results demonstrated that the accumulation ratio of hNRVs in the brain was significantly higher than that in other organs. Specifically, at 12 h postadministration, the DiR fluorescence signal intensity in the brain was 6.56 times, 4.21 times, 2.56 times, 8.43 times, and 4.24 times higher than those in the heart, liver, spleen, lungs, and kidneys, respectively. These data unequivocally highlight the excellent brain targeting ability of hNRVs, enabling the efficient delivery of drugs to the brain. Frozen brain sections were obtained for closer observation of the nanoparticle distribution. As shown in Figure 5F and Figure S3A, free DiI did not enter the tumor tissues. However, NK-EVs and hNRVs were distributed in the tumor tissues, confirming their brain targeting effect. Taken together, these data confirm our hypothesis that hNRVs have NK cell-like brain targeting characteristics, prolonged blood circulation, and the EPR effect, which facilitate RSL3 and NK-derived cytokine (IFN-γ and TNF-α) accumulation in glioma.

In addition, the distribution and metabolism of hNRVs in blood were also investigated. At various time points following drug administration, we measured the fluorescence signal intensity in the blood of the mice. A standard curve for DiI concentration detection was generated (Figure S3B). Within 30 min of drug administration, the fluorescence intensity was stronger in the RLP group, whereas the fluorescence signal in the hNRV group was relatively lower (Figure 5E). This suggested that, in the initial stages following drug administration, the drug was rapidly distributed into the blood and tissues of mice. In contrast, hNRVs exhibited faster distribution to the brain, potentially leading to a relatively lower drug concentration in the blood. Over time, at 12 h postadministration, the fluorescence intensity in the blood of the RLP group decreased significantly. This indicated that RLPs were gradually distributed from the blood to various tissues while being rapidly metabolized and eliminated by organs such as the liver and kidneys. In contrast, the fluorescence signal in the blood of the hNRV group remained at a relatively high level. This was attributed to the improved brain targeting and immune evasion capabilities of hNRVs, resulting in a longer retention time in the body and a slower rate of metabolism and elimination. At 48 h postadministration, the fluorescence signal of RLPs maintained a low but stable level, whereas the fluorescence signal in the blood of the hNRV group remained relatively high. This further confirmed the excellent brain targeting and longer retention time of hNRVs *in vivo*.

3.9. Antiglioma Efficacy *In Vivo*. Based on the enhanced tumor targeting effect, we then explored the *in vivo* antitumor efficacy of hNRVs in the orthotopic C6-luc glioma mouse model. The mice were randomly divided into 5 groups and intravenously injected with PBS (control), free RSL3, RLP, NK-EVs, and hNRVs. The therapy program was performed with the schedule in Figure 6A. Then, the tumor volume and progression were monitored by bioluminescence imaging. At day 7, strong fluorescence was observed in the PBS, RSL3 and RLPs groups, and the intensity of bioluminescence increased significantly over time, confirming that there was no significant inhibitory efficacy on the growth of tumors in the free RSL3 group, which was due to the rapid clearance of free drugs *in vivo* and poor tumor accumulation in glioma (Figure 6B). In addition, the mice treated with NK-EVs and RLPs exhibited limited tumor growth suppression. It was observed that the malignancy of the RLP group was similar to that of the PBS group, and the fluorescence intensity increased significantly over time. The mice in the NK-EV group showed significant recurrence on day 14, illustrating that regulating tumor ferroptosis or immunotherapy alone hardly effectively obtained effective antiglioma potency. In contrast, hNRVs efficiently inhibited recurrence with faint bioluminescence until day 23. In summary, hNRVs revealed the strongest tumor inhibition efficacy compared to the single NK-EVs and RLPs. Regarding the physiological state, the weight of mice treated with PBS and RSL3 decreased significantly, while the rate of the weight loss of mice treated with NK-EVs and hNRVs was relatively lower (Figure 6C). For RSL3-treated mice, this weight loss may have been due to the systemic side effects of RSL3 due to nonspecific circulation in the mice.[4] This phenomenon is consistent with NK-derived EVs enhancing the brain tumor targeting and therapeutic effect, thereby reducing the side effects of RSL3.

The capability of hNRVs to trigger enhanced tumor ablation encouraged us to further systematically explore whether the treatment increased the survival of mice bearing orthotopic C6 glioma. The survival curves are shown in Figure 6D. The median survival of mice treated with hNRVs was extended to 69 days, which is longer than other treatments including PBS (19 days), free RSL3 (18.5 days), NK-EVs (46.5 days), and RLPs (37 days). This extended survival may be related to the superior antitumor effect of hNRVs. Furthermore, H&E staining and TUNEL immunostaining were performed for the pathological analysis (Figure 6E). Compared to those of other groups, the tumor sections of mice treated with hNRV groups possessed the strongest cell disruption with the largest nucleus absence and produced the densest cell apoptosis, confirming their superior antiglioma potency. In addition, TUNEL expression in tumor tissues was significantly enhanced after treatment with hNRVs. All of these data suggested that hNRVs can effectively accumulate in tumor tissues to synergistically enhance tumor deposition by inducing tumor ferroptosis and amplified NK cell-induced immunotherapy.

3.10. Mechanism of hNRVs for Synergistic Ferroptosis-Immunotherapy. To uncover the underlying mechanism of synergistic ferroptosis-immunotherapy to suppress glioma growth, we first evaluated the hNRV-mediated ferroptosis pathway of tumor cells. Ferroptosis therapy (FT) of tumors aims to initiate programmed cell death by accumulated lipid peroxides (LPO). GPX4 is one of the master regulators of ferroptosis signaling pathways, and thus, GPX4 inhibition is the most powerful approach for inducing ferroptosis.[59]

https://doi.org/10.1021/acsami.4c04604
ACS Appl. Mater. Interfaces 2024, 16, 28193−28208

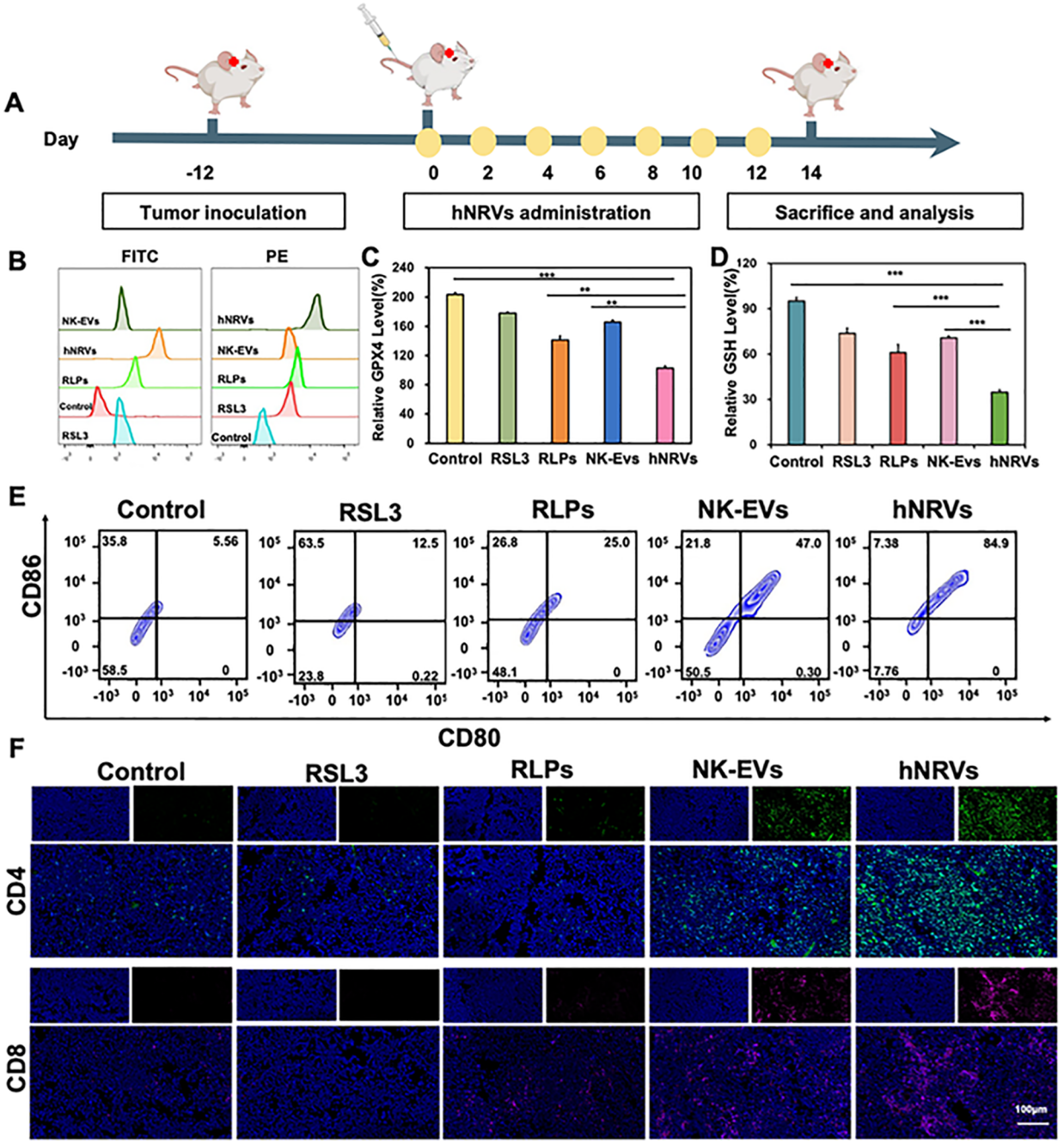

Figure 7. Synergistic mechanism of ferroptosis and immunotherapy induced by hNRVs *in vivo*. (A) Schematic illustration of animal experiment design on the synergistic effect of ferroptosis and immunotherapy. (B) Fluorescence distributions of the treated tumors stained with DCFH-DA and BODIPY C11-581/591. (C) Relative GPX4 and GSH (D) levels of the cells in the treated tumors. (E) Proportion of $CD80^+/CD86^+$ reflecting the ratio of mature DCs in the mouse spleen. (F) Immunofluorescence staining of anti-CD4 (green) and anti-CD8 (red) in the lymph node. Data were presented as means ± SD; $*p < 0.05$, $**p < 0.01$, and $***p < 0.001$; ns, not significant.

However, GPX4 is also critical in maintaining redox homeostasis in normal cells and tissues.[60] Selective inhibition of GPX4 in cancer cells is challenging because of the lack of advanced delivery systems for GPX4, limiting the clinical translation. Typically, under the slightly acidic TME, RSL3 released from the hNRVs generates ROS, leading to robust LPO accumulation and ferroptosis initiation. Furthermore, the IFN-γ secreted from NK-EVs cells inhibits system Xc^-, which downregulates the intracellular GSH/GPX4 and then promotes the ferroptosis acceleration. The corresponding mechanism was verified through the measurements of *in vivo* ROS, LPO, GPX4, and IFN-γ levels. Figure 7A shows the schematic illustration of the animal experimental design for determination for ferroptosis indicators and immune indicators in the C6 glioma-bearing mice after treatment (iv injection) of PBS (control), RLPs, NK-EVs, or hNRVs. Figure 7B and Figure S4A,B show the FC images with intratumor LPO and ROS accumulation stained by BODIPY C11-581/591 and DCFH-DA, respectively. It is found that hNRVs exhibit much stronger fluorescence than RLPs and NK-EVs, demonstrating the released RSL3-promoted ferroptosis. This result was consistent with the cellular level detection, confirming the

https://doi.org/10.1021/acsami.4c04604
ACS Appl. Mater. Interfaces 2024, 16, 28193−28208

occurrence of ferroptosis directly and the accurate glioma targeting indirectly by hNRVs. Because GSH acts as the cofactor of GPX4, GSH depletion can cause the inactivation of GPX4 and the accumulation of lipid peroxides and relevant degradation products.[61] As expected, hNRVs present much lower levels of GPX4 (Figure 7C) and GSH (Figure 7D) in the treated tumors than those of the other groups. Therefore, we speculated that the downregulation of GPX4 was due to the RSL3 inhibition and IFN-γ stimulation, which has also been shown in previous works.[62]

It has been proposed that apoptosis is an important mechanism in NK cell-based immunotherapy.[63] Perforin triggers the intrinsic pathway and elevates the release of cytochrome-c.[64] FASL triggers the extrinsic apoptotic pathway by activating caspase-3.[65,66] To confirm the cell death mechanism, we examined the expression of apoptosis-related proteins (caspase-3 and cytochrome-c) using IHC staining. As shown in Figure S4D, compared with the other groups, a large number of positive cells were observed in the hNRV and NK-EV groups, representing the apoptosis of tumor cells. Compared to the control group, the number of caspase-3-positive and cytochrome-c-positive cells increased significantly after 24 h of hNRV treatment. These results indicated that hNRVs could induce the apoptosis of the cancer cells by both the extrinsic and intrinsic apoptotic pathways.

Encouraged by hNRVs' superior ability to induce tumor ferroptosis, we then investigated the immunotherapeutic mechanism. The corresponding mechanism was verified by the measurements of *in vivo* immune indicators, including CD80/CD86, CD4/CD8, TNF-α, and IFN-γ. DC maturation is proven to be a pivotal process for initiating immune response by promoting effective antigen presentation and infiltration of cytotoxic T lymphocytes. The hallmarks of DC maturation are the high expression of stimulating factors (CD80, CD86, etc.).[67] As shown in Figure 7E, RLPs slightly induced DC maturation. On the contrary, the percentage of $CD80^+$ and $CD86^+$ DCs after the treatment with hNRVs was obviously higher than those of other groups, with 2.28-fold and 3.60-fold increases compared to the control group (Figure S4C), respectively. In addition, DC maturation would activate cytotoxic $CD8^+$ T cells and $CD4^+$ T cells. Subsequently, the infiltration of $CD8^+$ and $CD4^+$ T lymphocytes in tumor tissues was analyzed to evaluate the antitumor immune response (Figure 7F). Compared with other groups, hNRVs had the highest percentage of $CD4^+$ and $CD8^+$ T cells in tumor tissues. These results confirmed that hNRVs can effectively facilitate the infiltration of $CD4^+$ and $CD8^+$ T cell lymphocytes in tumors. NK-EVs have been confirmed to contain cytokines such as IFN-γ. Cytokines including IFN-γ and TNF-α are the key biomarkers released by tumor-infiltrating T cells, which can activate an antitumor immune response. Therefore, we also detected the expression of TNF-α and IFN-γ in tumors using an ELISA assay. Results demonstrated the remarkably upregulated levels of TNF-α and IFN-γ in mice receiving hNRVs (Figure S4E,F). Typically, activating $CD8^+$ T cells would further enhance ferroptosis-specific lipid peroxidation in tumor cells by releasing IFN-γ. Therefore, we demonstrated that our biomimetic delivery systems could effectively induce GPX4-mediated ferroptosis and increase the NK-related cytokine accumulation in tumors, thereby enabling reversal of the immunosuppressive TME and boosting NK-induced antitumor immune effects. Such a positive loop between C6 glioma ferroptosis and NK-mediated immunotherapy can be enhanced by targeted hNRV systems.

In summary, the synergistic effect of ferroptosis and immunotherapy in our system arises from several key mechanisms. First, the release of FASL from NK cells effectively lyses tumor cells, creating a favorable microenvironment for ferroptosis. Second, RSL3 downregulates the expression of GPX4 in tumor cells, leading to the accumulation of lipid peroxidation (LPO) and reactive oxygen species (ROS), which are critical for ferroptosis. Importantly, the accumulation of cytokines such as IFN-γ and TNF-α in the tumor microenvironment stimulates the maturation of dendritic cells and effectively induces the inactivation of GPX4. This inactivation further promotes lipid peroxidation and sensitizes the tumor cells to ferroptosis. In this way, immunotherapy not only enhances the direct killing effect of ferroptosis but also indirectly promotes the occurrence of ferroptosis by modulating the tumor microenvironment. Moreover, the EPR effect and tumor homing characteristics of NK exosomes ensure that hNRVs actively accumulate in tumors, maximizing the local concentration of therapeutic agents and minimizing off-target effects. This targeted delivery approach further enhances the synergistic effect between ferroptosis and immunotherapy.

Our study demonstrates that the customized hNRV platform can effectively enhance the therapeutic effect of ferroptosis therapy and immunotherapy through their synergistic actions. By targeting tumor cells specifically and modulating the tumor microenvironment, we aim to achieve better therapeutic outcomes without causing additional side effects on healthy organs. We believe that this approach has the potential to revolutionize cancer treatment and improve patient outcomes.

3.11. Safety Evaluation. The biosafety of the different treated groups was determined during treatment. The body weights of mice during treatments are shown in Figure S5A. No significant changes in body weight were observed across all of the experimental groups. Considering the *in vivo* administration, a hemolytic test was conducted on liposomes. All of the formulations demonstrated excellent blood compatibility at this concentration. Finally, a systematic investigation of *in vivo* toxicology and potential side effects was conducted in normal mice. ALT, AST, and CREA are closely associated with liver and kidney functions in mice (Figure S5B–D). The hematological analysis revealed that the indexes of each group were relatively stable compared to the control group, indicating the absence of hepatotoxicity and nephrotoxicity. In addition, the main organs of mice (heart, liver, spleen, lung, and kidney) were harvested for H&E staining (Figure S5E). Compared with the control group, all treatment groups exhibited no significant pathologic abnormalities, indicating the absence of obvious toxicity to mouse organs, as expected. All of these data confirmed that the preparations used possessed good biocompatibility and biosafety and had potential for the treatment of glioma *in vivo*.

4. CONCLUSIONS

In this study, we introduce hNRVs, an advanced hybrid biomimetic nanovesicle designed to enhance ferroptosis and immunotherapy for brain glioma treatment. This delivery system, loaded with ferroptosis inducers and immune activators, integrates active targeting, drug release, immune activation, and selective lipid peroxidation. Prepared via a simple and robust process, hNRVs encapsulate RSL3 in RLPs

https://doi.org/10.1021/acsami.4c04604
ACS Appl. Mater. Interfaces 2024, 16, 28193−28208

and integrate with NK-EVs. Characterization demonstrates excellent drug loading, uniform size, and stability. CLSM and flow cytometry demonstrated cellular uptake and immune evasion. Ferroptosis is confirmed through ROS, LPO, GSH, and GPX4 levels, while immunotherapeutic effects are shown through CD80/CD86 expression and cytokine measurement. In orthotopic glioma mice, hNRV-induced therapy demonstrates targeting, efficacy, and biosafety via live imaging, IHC, IF, and ELISA. The mechanism of hNRVs *in vivo* was determined by assessing ROS, LPO, GPX4, and GSH levels, analyzing tumor-infiltrating DCs with anti-CD86/CD80, examining $CD8^+$ T cells with anti-CD4-FITC/CD8-PE, and measuring TNF-α and IFN-γ secretion. Our study highlights the potential of hNRVs in coordinating ferroptosis and immunotherapy, offering a promising multimodal approach for glioma.

■ ASSOCIATED CONTENT

Supporting Information

The Supporting Information is available free of charge at https://pubs.acs.org/doi/10.1021/acsami.4c04604.

Flow cytometry of the activated NK cell marker NKG2C and CD16; total protein concentration, zeta potential, and stability of hNRVs; encapsulation efficiency and loading efficiency of RLPs and hNRVs; cellular uptake of hNRVs in bEnd.3 and C6 cells; fluorescence intensity of the lower chamber in the BBB and BBTB models; viability of C6 cells after various treatments; *in vitro* immune escape capability of hNRVs; illustration of Transwell to coculture C6 cells and immature dendritic cells; representative fluorescence images of hNRVs in glioma at 12 h after administration; standard curve for DiI concentration determination; synergistic mechanism of ferroptosis and immunotherapy induced by hNRVs *in vivo*; biosafety evaluation of hNRVs (PDF)

■ AUTHOR INFORMATION

Corresponding Authors

Meiyan Yang − *State Key Laboratory of Toxicology and Medical Countermeasures, Beijing Institute of Pharmacology and Toxicology, Beijing 100850, China*; Email: ymyzi@163.com

Yang Yang − *State Key Laboratory of Toxicology and Medical Countermeasures, Beijing Institute of Pharmacology and Toxicology, Beijing 100850, China*; orcid.org/0000-0002-3195-2069; Email: jiamusi101@126.com

Chunsheng Gao − *State Key Laboratory of Toxicology and Medical Countermeasures, Beijing Institute of Pharmacology and Toxicology, Beijing 100850, China*; Email: gaocs@bmi.ac.cn

Authors

Wenyan Hao − *State Key Laboratory of Toxicology and Medical Countermeasures, Beijing Institute of Pharmacology and Toxicology, Beijing 100850, China*

Nan Sun − *State Key Laboratory of Toxicology and Medical Countermeasures, Beijing Institute of Pharmacology and Toxicology, Beijing 100850, China*

Yueyue Fan − *State Key Laboratory of Toxicology and Medical Countermeasures, Beijing Institute of Pharmacology and Toxicology, Beijing 100850, China*

Mengyu Chen − *State Key Laboratory of Toxicology and Medical Countermeasures, Beijing Institute of Pharmacology and Toxicology, Beijing 100850, China*

Qianqian Liu − *State Key Laboratory of Toxicology and Medical Countermeasures, Beijing Institute of Pharmacology and Toxicology, Beijing 100850, China*

Complete contact information is available at: https://pubs.acs.org/10.1021/acsami.4c04604

Notes

All procedures involving the care and handling of animals were carried out with the approval of the Animal Care and Use Ethics Committee of the Beijing Institute of Pharmacology and Toxicology (Beijing, China). This committee also approved all animal-related experiments in the current study (No. IACUC-DWZX-2020-646).

The authors declare no competing financial interest.

■ ACKNOWLEDGMENTS

This work was supported by the Natural Science Foundation of China (82304405), the China Postdoctoral Science Foundation (2023M744314), and the Beijing Natural Science Foundation (7234405). The authors thank LetPub (www.letpub.com) for its linguistic assistance during the preparation of this manuscript.

■ REFERENCES

(1) Zhu, Y.; Liang, J.; Gao, C.; Wang, A.; Xia, J.; Hong, C.; Zhong, Z.; Zuo, Z.; Kim, J.; Ren, H.; Li, S.; Wang, Q.; Zhang, F.; Wang, J. Multifunctional ginsenoside Rg3-based liposomes for glioma targeting therapy. *J. Controlled Release* **2021**, *330*, 641−657.

(2) Fan, Y.; Cui, Y.; Hao, W.; Chen, M.; Liu, Q.; Wang, Y.; Yang, M.; Li, Z.; Gong, W.; Song, S.; Yang, Y.; Gao, C. Carrier-free highly drug-loaded biomimetic nanosuspensions encapsulated by cancer cell membrane based on homology and active targeting for the treatment of glioma. *Bioact Mater.* **2021**, *6*, 4402−4414.

(3) Lara-Velazquez, M.; Al-Kharboosh, R.; Jeanneret, S.; Vazquez-Ramos, C.; Mahato, D.; Tavanaiepour, D.; Rahmathulla, G.; Quinones-Hinojosa, A. Advances in Brain Tumor Surgery for Glioblastoma in Adults. *Brain Sci.* **2017**, *7*, 166.

(4) Yang, Z.; Du, Y.; Sun, Q.; Peng, Y.; Wang, R.; Zhou, Y.; Wang, Y.; Zhang, C.; Qi, X. Albumin-Based Nanotheranostic Probe with Hypoxia Alleviating Potentiates Synchronous Multimodal Imaging and Phototherapy for Glioma. *ACS Nano* **2020**, *14*, 6191−6212.

(5) Alifieris, C.; Trafalis, D. T. Glioblastoma multiforme: Pathogenesis and treatment. *Pharmacol Ther.* **2015**, *152*, 63−82.

(6) Kadiyala, P.; Li, D.; Nuñez, F. M.; Altshuler, D.; Doherty, R.; Kuai, R.; Yu, M.; Kamran, N.; Edwards, M.; Moon, J. J.; Lowenstein, P. R.; Castro, M. G.; Schwendeman, A. High-Density Lipoprotein-Mimicking Nanodiscs for Chemo-immunotherapy against Glioblastoma Multiforme. *ACS Nano* **2019**, *13*, 1365−1384.

(7) Peng, J.; Chen, F.; Liu, Y.; Zhang, F.; Cao, L.; You, Q.; Yang, D.; Chang, Z.; Ge, M.; Li, L.; Wang, Z.; Mei, Q.; Shao, D.; Chen, M.; Dong, W. F. A light-driven dual-nanotransformer with deep tumor penetration for efficient chemo-immunotherapy. *Theranostics.* **2022**, *12*, 1756−1768.

(8) Kim, S. S.; Rait, A.; Kim, E.; Pirollo, K. F.; Nishida, M.; Farkas, N.; Dagata, J. A.; Chang, E. H. A nanoparticle carrying the p53 gene targets tumors including cancer stem cells, sensitizes glioblastoma to chemotherapy and improves survival. *ACS Nano* **2014**, *8*, 5494−5514.

(9) Ni, D.; Zhang, J.; Bu, W.; Xing, H.; Han, F.; Xiao, Q.; Yao, Z.; Chen, F.; He, Q.; Liu, J.; Zhang, S.; Fan, W.; Zhou, L.; Peng, W.; Shi, J. Dual-targeting upconversion nanoprobes across the blood-brain barrier for magnetic resonance/fluorescence imaging of intracranial glioblastoma. *ACS Nano* **2014**, *8*, 1231−1242.

(10) Chen, X.; Kang, R.; Kroemer, G.; Tang, D. Broadening horizons: the role of ferroptosis in cancer. *Nat. Rev. Clin Oncol.* **2021**, *18*, 280−296.
(11) Huang, L.; Zhu, J.; Xiong, W.; Feng, J.; Yang, J.; Lu, X.; Lu, Y.; Zhang, Q.; Yi, P.; Feng, Y.; Guo, S.; Qiu, X.; Xu, Y.; Shen, Z. Tumor-Generated Reactive Oxygen Species Storm for High-Performance Ferroptosis Therapy. *ACS Nano* **2023**, *17*, 11492−11506.
(12) Chen, J. J.; Galluzzi, L. Fighting Resilient Cancers with Iron. *Trends Cell Biol.* **2018**, *28*, 77−78.
(13) Gao, M.; Deng, J.; Liu, F.; Fan, A.; Wang, Y.; Wu, H.; Ding, D.; Kong, D.; Wang, Z.; Peer, D.; Zhao, Y. Triggered ferroptotic polymer micelles for reversing multidrug resistance to chemotherapy. *Biomaterials.* **2019**, *223*, No. 119486.
(14) Guo, Q.; Li, X.; Zhou, W.; Chu, Y.; Chen, Q.; Zhang, Y.; Li, C.; Chen, H.; Liu, P.; Zhao, Z.; Wang, Y.; Zhou, Z.; Luo, Y.; Li, C.; You, H.; Song, H.; Su, B.; Zhang, T.; Sun, T.; Jiang, C. Sequentially Triggered Bacterial Outer Membrane Vesicles for Macrophage Metabolism Modulation and Tumor Metastasis Suppression. *ACS Nano* **2021**, *15*, 13826−13838.
(15) Gao, Z.; Zhang, J.; Hou, Y.; Lu, J.; Liang, J.; Gao, Y.; Li, B.; Gao, S.; Zhao, Y.; Gao, M.; Chen, J. Boosting the synergism between cancer ferroptosis and immunotherapy via targeted stimuli-responsive liposomes. *Biomaterials.* **2024**, *305*, No. 122442.
(16) Shi, W.; Feng, W.; Li, S.; Cui, Y.; Liu, S.; Jiang, H.; Liu, Y.; Zhang, H. Ferroptosis and Necroptosis Produced Autologous Tumor Cell Lysates Co-Delivering with Combined Immnoadjuvants as Personalized In Situ Nanovaccines for Antitumor Immunity. *ACS Nano* **2023**, *17*, 14475−14493.
(17) Nie, T.; Liu, H.; Fang, Z.; Zheng, Y.; Zhang, R.; Xu, X.; Liu, S.; Wu, J. Tumor Microenvironment Mediated Spermidine-Metal-Immunopeptide Nanocomplex for Boosting Ferroptotic Immunotherapy of Lymphoma. *ACS Nano* **2023**, *17*, 10925−10937.
(18) Wiernicki, B.; Maschalidi, S.; Pinney, J.; Adjemian, S.; Vanden Berghe, T.; Ravichandran, K. S.; Vandenabeele, P. Cancer cells dying from ferroptosis impede dendritic cell-mediated anti-tumor immunity. *Nat. Commun.* **2022**, *13*, 3676.
(19) Yang, W.; Deng, C.; Shi, X.; Xu, Y.; Dai, C.; Wang, H.; Bian, K.; Cui, T.; Zhang, B. Structural and Molecular Fusion MRI Nanoprobe for Differential Diagnosis of Malignant Tumors and Follow-Up Chemodynamic Therapy. *ACS Nano* **2023**, *17*, 4009−4022.
(20) Tong, F.; Hu, H.; Xu, Y.; Zhou, Y.; Xie, R.; Lei, T.; Du, Y.; Yang, W.; He, S.; Huang, Y.; Gong, T.; Gao, H. Hollow copper sulfide nanoparticles carrying ISRIB for the sensitized photothermal therapy of breast cancer and brain metastases through inhibiting stress granule formation and reprogramming tumor-associated macrophages. *Acta Pharm. Sin B* **2023**, *13*, 3471−3488.
(21) Chen, X.; Yu, C.; Kang, R.; Kroemer, G.; Tang, D. Cellular degradation systems in ferroptosis. *Cell Death Differ.* **2021**, *28*, 1135−1148.
(22) Wang, B.; Wang, Y.; Zhang, J.; Hu, C.; Jiang, J.; Li, Y.; Peng, Z. ROS-induced lipid peroxidation modulates cell death outcome: mechanisms behind apoptosis, autophagy, and ferroptosis. *Arch. Toxicol.* **2023**, *97*, 1439−1451.
(23) Qi, J.; Kim, J. W.; Zhou, Z.; Lim, C. W.; Kim, B. Ferroptosis Affects the Progression of Nonalcoholic Steatohepatitis via the Modulation of Lipid Peroxidation-Mediated Cell Death in Mice. *Am. J. Pathol.* **2020**, *190*, 68−81.
(24) Guo, X.; Liu, F.; Deng, J.; Dai, P.; Qin, Y.; Li, Z.; Wang, B.; Fan, A.; Wang, Z.; Zhao, Y. Electron-Accepting Micelles Deplete Reduced Nicotinamide Adenine Dinucleotide Phosphate and Impair Two Antioxidant Cascades for Ferroptosis-Induced Tumor Eradication. *ACS Nano* **2020**, *14*, 14715−14730.
(25) Li, H.; Feng, Y.; Luo, Q.; Li, Z.; Li, X.; Gan, H.; Gu, Z.; Gong, Q.; Luo, K. Stimuli-activatable nanomedicine meets cancer theranostics. *Theranostics.* **2023**, *13*, 5386−5417.
(26) Alfaifi, A. A.; Heyder, R. S.; Bielski, E. R.; Almuqbil, R. M.; Kavdia, M.; Gerk, P. M.; da Rocha, S. R. P. Megalin-targeting liposomes for placental drug delivery. *J. Controlled Release* **2020**, *324*, 366−378.
(27) Zhu, L.; Kalimuthu, S.; Gangadaran, P.; Oh, J. M.; Lee, H. W.; Baek, S. H.; Jeong, S. Y.; Lee, S. W.; Lee, J.; Ahn, B. C. Exosomes Derived From Natural Killer Cells Exert Therapeutic Effect in Melanoma. *Theranostics.* **2017**, *7*, 2732−2745.
(28) Gang, M.; Wong, P.; Berrien-Elliott, M. M.; Fehniger, T. A. Memory-like natural killer cells for cancer immunotherapy. *Semin Hematol.* **2020**, *57*, 185−193.
(29) Chiossone, L.; Dumas, P. Y.; Vienne, M.; Vivier, E. Natural killer cells and other innate lymphoid cells in cancer. *Nat. Rev. Immunol.* **2018**, *18*, 671−688.
(30) Quintino-de-Carvalho, I. L.; Goncalves-Pereira, M. H.; Faria Ramos, M.; de Aguiar Milhim, B. H. G.; Da Costa, U. L.; Santos, E. G.; Nogueira, M. L.; Da Costa Santiago, H. Type 1 Innate Lymphoid Cell and Natural Killer Cells Are Sources of Interferon-gamma and Other Inflammatory Cytokines Associated With Distinct Clinical Presentation in Early Dengue Infection. *J. Infect Dis.* **2022**, *225*, 84−93.
(31) Vanek, O.; Kalouskova, B.; Abreu, C.; Nejadebrahim, S.; Skorepa, O. Natural killer cell-based strategies for immunotherapy of cancer. *Adv. Protein Chem. Struct Biol.* **2022**, *129*, 91−133.
(32) Wang, W.; Green, M.; Choi, J. E.; Gijon, M.; Kennedy, P. D.; Johnson, J. K.; Liao, P.; Lang, X.; Kryczek, I.; Sell, A.; Xia, H.; Zhou, J.; Li, G.; Li, J.; Li, W.; Wei, S.; Vatan, L.; Zhang, H.; Szeliga, W.; Gu, W.; Liu, R.; Lawrence, T. S.; Lamb, C.; Tanno, Y.; Cieslik, M.; Stone, E.; Georgiou, G.; Chan, T. A.; Chinnaiyan, A.; Zou, W. CD8(+) T cells regulate tumour ferroptosis during cancer immunotherapy. *Nature.* **2019**, *569*, 270−274.
(33) Bai, L.; Liu, Y.; Guo, K.; Zhang, K.; Liu, Q.; Wang, P.; Wang, X. Ultrasound Facilitates Naturally Equipped Exosomes Derived from Macrophages and Blood Serum for Orthotopic Glioma Treatment. *ACS Appl. Mater. Interfaces.* **2019**, *11*, 14576−14587.
(34) Li, H.; Sun, J.; Zhu, H.; Wu, H.; Zhang, H.; Gu, Z.; Luo, K. Recent advances in development of dendritic polymer-based nanomedicines for cancer diagnosis. *Wiley Interdiscip. Rev. Nanomed. Nanobiotechnol.* **2021**, *13*, No. e1670.
(35) Hu, M.; Zhang, J.; Kong, L.; Yu, Y.; Hu, Q.; Yang, T.; Wang, Y.; Tu, K.; Qiao, Q.; Qin, X.; Zhang, Z. Immunogenic Hybrid Nanovesicles of Liposomes and Tumor-Derived Nanovesicles for Cancer Immunochemotherapy. *ACS Nano* **2021**, *15*, 3123−3138.
(36) Sun, M.; Yang, J.; Fan, Y.; Zhang, Y.; Sun, J.; Hu, M.; Sun, K.; Zhang, J. Beyond Extracellular Vesicles: Hybrid Membrane Nanovesicles as Emerging Advanced Tools for Biomedical Applications. *Adv. Sci.* **2023**, *10*, No. 2303617.
(37) Kokowski, K.; Stangl, S.; Seier, S.; Hildebrandt, M.; Vaupel, P.; Multhoff, G. Radiochemotherapy combined with NK cell transfer followed by second-line PD-1 inhibition in a patient with NSCLC stage IIIb inducing long-term tumor control: a case study. *Strahlenther Onkol.* **2019**, *195*, 352−361.
(38) Théry, C.; Amigorena, S.; Raposo, G.; Clayton, A. Isolation and characterization of exosomes from cell culture supernatants and biological fluids. *Curr. Protoc. Cell Biol.* **2006**, *30*, 3−22.
(39) Wiraja, C.; Mathiyazhakan, M.; Movahedi, F.; Upputuri, P. K.; Cheng, Y.; Pramanik, M.; Yang, L.; Becker, D. L.; Xu, C. Near-infrared light-sensitive liposomes for enhanced plasmid DNA transfection. *Bioeng Transl Med.* **2016**, *1*, 357−364.
(40) Fais, S. NK cell-released exosomes: Natural nanobullets against tumors. *Oncoimmunology.* **2013**, *2*, No. e22337.
(41) Lugini, L.; Cecchetti, S.; Huber, V.; Luciani, F.; Macchia, G.; Spadaro, F.; Paris, L.; Abalsamo, L.; Colone, M.; Molinari, A.; Podo, F.; Rivoltini, L.; Ramoni, C.; Fais, S. Immune surveillance properties of human NK cell-derived exosomes. *J. Immunol.* **2012**, *189*, 2833−2842.
(42) Hao, W.; Cui, Y.; Fan, Y.; Chen, M.; Yang, G.; Wang, Y.; Yang, M.; Li, Z.; Gong, W.; Yang, Y.; Gao, C. Hybrid membrane-coated nanosuspensions for multi-modal anti-glioma therapy via drug and antigen delivery. *J. Nanobiotechnol.* **2021**, *19*, 378.
(43) Ju, C.; Wen, Y.; Zhang, L.; Wang, Q.; Xue, L.; Shen, J.; Zhang, C. Neoadjuvant Chemotherapy Based on Abraxane/Human Neu-

https://doi.org/10.1021/acsami.4c04604
ACS Appl. Mater. Interfaces 2024, 16, 28193−28208

trophils Cytopharmaceuticals with Radiotherapy for Gastric Cancer. *Small* **2019**, *15*, No. 1804191.
(44) Xue, J.; Zhao, Z.; Zhang, L.; Xue, L.; Shen, S.; Wen, Y.; Wei, Z.; Wang, L.; Kong, L.; Sun, H.; Ping, Q.; Mo, R.; Zhang, C. Neutrophil-mediated anticancer drug delivery for suppression of postoperative malignant glioma recurrence. *Nat. Nanotechnol.* **2017**, *12*, 692−700.
(45) Deng, G.; Peng, X.; Sun, Z.; Zheng, W.; Yu, J.; Du, L.; Chen, H.; Gong, P.; Zhang, P.; Cai, L.; Tang, B. Z. Natural-Killer-Cell-Inspired Nanorobots with Aggregation-Induced Emission Characteristics for Near-Infrared-II Fluorescence-Guided Glioma Theranostics. *ACS Nano* **2020**, *14*, 11452−11462.
(46) Gross, C.; Schmidt-Wolf, I. G.; Nagaraj, S.; Gastpar, R.; Ellwart, J.; Kunz-Schughart, L. A.; Multhoff, G. Heat shock protein 70-reactivity is associated with increased cell surface density of CD94/CD56 on primary natural killer cells. *Cell Stress Chaperones.* **2003**, *8*, 348−360.
(47) Gross, C.; Hansch, D.; Gastpar, R.; Multhoff, G. Interaction of heat shock protein 70 peptide with NK cells involves the NK receptor CD94. *Biol. Chem.* **2003**, *384*, 267.
(48) Guo, S.; Xiong, W.; Zhu, J.; Feng, J.; Zhou, R.; Fan, Q.; Zhang, Q.; Li, Z.; Yang, J.; Zhou, H.; Yi, P.; Feng, Y.; Yang, S.; Qiu, X.; Xu, Y.; Shen, Z. A STING pathway-activatable contrast agent for MRI-guided tumor immunoferroptosis synergistic therapy. *Biomaterials.* **2023**, *302*, No. 122300.
(49) Chen, Q.; Shan, X.; Shi, S.; Jiang, C.; Li, T.; Wei, S.; Zhang, X.; Sun, G.; Liu, J. Tumor microenvironment-responsive polydopamine-based core/shell nanoplatform for synergetic theranostics. *J. Mater. Chem. B* **2020**, *8*, 4056−4066.
(50) Miao, D.; Jiang, M.; Liu, Z.; Gu, G.; Hu, Q.; Kang, T.; Song, Q.; Yao, L.; Li, W.; Gao, X.; Sun, M.; Chen, J. Co-administration of dual-targeting nanoparticles with penetration enhancement peptide for antiglioblastoma therapy. *Mol. Pharmaceutics* **2014**, *11*, 90−101.
(51) Fitzner, D.; Schnaars, M.; van Rossum, D.; Krishnamoorthy, G.; Dibaj, P.; Bakhti, M.; Regen, T.; Hanisch, U. K.; Simons, M. Selective transfer of exosomes from oligodendrocytes to microglia by macropinocytosis. *J. Cell Sci.* **2011**, *124*, 447−458.
(52) Escrevente, C.; Keller, S.; Altevogt, P.; Costa, J. Interaction and uptake of exosomes by ovarian cancer cells. *BMC Cancer.* **2011**, *11*, 108.
(53) Quail, D. F.; Joyce, J. A. Microenvironmental regulation of tumor progression and metastasis. *Nat. Med.* **2013**, *19*, 1423−1437.
(54) Quail, D. F.; Joyce, J. A. The Microenvironmental Landscape of Brain Tumors. *Cancer Cell.* **2017**, *31*, 326−341.
(55) Wang, J.; Tang, W.; Yang, M.; Yin, Y.; Li, H.; Hu, F.; Tang, L.; Ma, X.; Zhang, Y.; Wang, Y. Inflammatory tumor microenvironment responsive neutrophil exosomes-based drug delivery system for targeted glioma therapy. *Biomaterials.* **2021**, *273*, No. 120784.
(56) Wan, Z.; Huang, H.; West, R. E., 3rd; Zhang, M.; Zhang, B.; Cai, X.; Zhang, Z.; Luo, Z.; Chen, Y.; Zhang, Y.; Xie, W.; Yang, D.; Nolin, T. D.; Wang, J.; Li, S.; Sun, J. Overcoming pancreatic cancer immune resistance by codelivery of CCR2 antagonist using a STING-activating gemcitabine-based nanocarrier. *Mater. Today (Kidlington).* **2023**, *62*, 33−50.
(57) Choi, B.; Park, W.; Park, S. B.; Rhim, W. K.; Han, D. K. Recent trends in cell membrane-cloaked nanoparticles for therapeutic applications. *Methods.* **2020**, *177*, 2−14.
(58) Falvo, P.; Orecchioni, S.; Hillje, R.; Raveane, A.; Mancusco, P.; Camisaschi, C. Correction: Cyclophosphamide and Vinorelbine Activate Stem-Like CD8(+) T Cells and Improve Anti-PD-1 Efficacy in Triple-Negative Breast Cancer. *Cancer Res.* **2021**, *81*, 3426.
(59) Yang, W. S.; SriRamaratnam, R.; Welsch, M. E.; Shimada, K.; Skouta, R.; Viswanathan, V. S.; Cheah, J. H.; Clemons, P. A.; Shamji, A. F.; Clish, C. B.; Brown, L. M.; Girotti, A. W.; Cornish, V. W.; Schreiber, S. L.; Stockwell, B. R. Regulation of ferroptotic cancer cell death by GPX4. *Cell.* **2014**, *156*, 317−331.
(60) Rodriguez, R.; Schreiber, S. L.; Conrad, M. Persister cancer cells: Iron addiction and vulnerability to ferroptosis. *Mol. Cell* **2022**, *82*, 728−740.
(61) Zhang, P.; Rashidi, A.; Zhao, J.; Silvers, C.; Wang, H.; Castro, B.; Ellingwood, A.; Han, Y.; Lopez-Rosas, A.; Zannikou, M.; Dmello, C.; Levine, R.; Xiao, T.; Cordero, A.; Sonabend, A. M.; Balyasnikova, I. V.; Lee-Chang, C.; Miska, J.; Lesniak, M. S. STING agonist-loaded, CD47/PD-L1-targeting nanoparticles potentiate antitumor immunity and radiotherapy for glioblastoma. *Nat. Commun.* **2023**, *14*, 1610.
(62) Sun, Z.; Wang, Z.; Wang, T.; Wang, J.; Zhang, H.; Li, Z.; Wang, S.; Sheng, F.; Yu, J.; Hou, Y. Biodegradable MnO-Based Nanoparticles with Engineering Surface for Tumor Therapy: Simultaneous Fenton-Like Ion Delivery and Immune Activation. *ACS Nano* **2022**, *16*, 11862−11875.
(63) Deng, J.; Xu, W.; Lei, S.; Li, W.; Li, Q.; Li, K.; Lyu, J.; Wang, J.; Wang, Z. Activated Natural Killer Cells-Dependent Dendritic Cells Recruitment and Maturation by Responsive Nanogels for Targeting Pancreatic Cancer Immunotherapy. *Small* **2022**, *18*, No. 2203114.
(64) Kim, S.; Li, S.; Jangid, A. K.; Park, H. W.; Lee, D.-J.; Jung, H.-S.; Kim, K. Surface Engineering of Natural Killer Cells with CD44-targeting Ligands for Augmented Cancer Immunotherapy. *Small* **2023**, No. 2306738.
(65) Augstein, P.; Heinke, P.; Schober, C.; Salzsieder, E. Impact of cytokine- and FasL-induced apoptosis in the beta-cell line NIT-1. *Horm Metab Res.* **2009**, *41*, 207−212.
(66) Lee, H. W.; Singh, T. D.; Lee, S. W.; Ha, J. H.; Rehemtulla, A.; Ahn, B. C.; Jeon, Y. H.; Lee, J. Evaluation of therapeutic effects of natural killer (NK) cell-based immunotherapy in mice using in vivo apoptosis bioimaging with a caspase-3 sensor. *FASEB J.* **2014**, *28*, 2932−2941.
(67) Swietek, M.; Ma, Y. H.; Wu, N. P.; Paruzel, A.; Tokarz, W.; Horak, D. Tannic Acid Coating Augments Glioblastoma Cellular Uptake of Magnetic Nanoparticles with Antioxidant Effects. *Nanomaterials (Basel).* **2022**, *12*, 1310.

https://doi.org/10.1021/acsami.4c04604
ACS Appl. Mater. Interfaces 2024, 16, 28193−28208